

© 2025 IEEE. Personal use of this material is permitted. Permission from IEEE must be obtained for all other uses, including reprinting/republishing this material for advertising or promotional purposes, collecting new collected works for resale or redistribution to servers or lists, or reuse of any copyrighted component of this work in other works. This work has been submitted to the IEEE for possible publication. Copyright may be transferred without notice, after which this version may no longer be accessible.

arXiv:2505.14486v2 [cs.RO] 25 May 2025

# Robust Immersive Bilateral Teleoperation of Beyond-Human-Scale Systems with Enhanced Transparency and Sense of Embodiment

Mahdi Hejrati , Pauli Mustalahti , and Jouni Mattila 

**Abstract**—In human-in-the-loop systems such as teleoperation, especially those involving heavy-duty manipulators, achieving high task performance requires both robust control and strong human engagement. This paper presents a bilateral teleoperation framework for beyond-human-scale robotic systems that enhances the transparency and the operator’s sense of embodiment (SoE), specifically, the senses of agency and self-location, through an immersive virtual reality interface and distributed haptic feedback. To support this embodiment and establish high level of motion and force transparency, we develop a force-sensorless, robust control architecture that tackles input nonlinearities, master-surrogate asymmetries, unknown uncertainties, and arbitrary time delays. A human-robot augmented dynamic model is integrated into the control loop to enhance human-adaptability of the controller. Theoretical analysis confirms semi-global uniform ultimate boundedness of the closed-loop system, guaranteeing the robustness to the real-world uncertainties. Extensive real-world experiments demonstrate high accuracy tracking under up to 1:13 motion scaling and 1:1000 force scaling, showcasing the significance of the results. Additionally, the stability-transparency tradeoff for motion tracking and force reflection and tracking is established up to 150 ms of one-way fix and time-varying communication delays. The results of user study with 10 participants (9 male and 1 female) demonstrate that the system can imply a good level of SoE (76.4%), at the same time is very user friendly with no gender limitation. These results are significant given the scale and weight of the heavy-duty manipulators.

**Index Terms**—Bilateral teleoperation control, time delay, transparency, virtual reality, haptic display, sense of embodiment

## I. INTRODUCTION

TELEOPERATED robotic systems, first introduced by Goertz in the 1940s [1], integrate human cognitive abilities with control-theoretic approaches to enable remote operation of robots in environments that are hazardous, unstructured, or otherwise unsuitable for direct human presence. In scenarios where use of fully autonomous systems remain impractical or unsafe, teleoperation offers a robust and flexible alternative, with proven effectiveness across a wide range of domains [2]–[4]. One field with significant untapped potential for teleoperation is heavy-duty robotic operation, particularly through the use of heavy-duty hydraulic manipulators (HHMs). These machines are already widely deployed in industries such as mining, construction, and forestry, where they handle physically intensive tasks in dynamic and often dangerous environments. By integrating human sensorimotor skills with the power and scale of HHMs, teleoperation equips HHMs with

beyond human capabilities, while providing a reliable medium for intuitive human-to-HHM skill transfer [5], addressing a key bottleneck in their automation [6].

Despite the advantages of teleoperation, task performance often deteriorates during remote operation due to factors such as master-surrogate mismatches, communication delays, and non-intuitive human-machine interfaces that can cause cyber sicknesses [7]. These challenges become even more pronounced when teleoperating HHMs, whose scale, dynamics, and mechanical complexity make them significantly less tractable than lightweight robotic systems. Such issues disrupt the operator’s natural sensorimotor loop and can impair proprioceptive perception, especially with visuo-haptic feedback, leading to a loss of intuitiveness in the teleoperation experience. One effective approach to mitigate these effects is enhancing the operator’s sense of *presence* [8], defined as the subjective experience of being physically situated at the remote site, which, in the context of teleoperation, is more precisely referred to as the sense of *telepresence* (SoT) [9], [10]. Nonetheless, enhancing telepresence alone is not sufficient to ensure high-quality task execution in teleoperation by a human operator.

Slater (2009) [11] argued that Place Illusion—his proposed refinement of the term “presence”—is not sufficient on its own for users to behave realistically in virtual environments. He introduced the concept of Plausibility Illusion, defined as the illusion that events occurring in the virtual environment are actually happening. According to Slater, both Place Illusion and Plausibility Illusion must co-occur for users to generate realistic responses within the virtual context. Building on this framework, Kilteni et al. (2012) [12] emphasized that realistic actions in virtual environments are closely linked to the sense of embodiment (SoE). Within the concept of teleoperation, SoE is defined as a psychological state in which the operator experiences the surrogate as an extension of their own body. According to [12], [13], SoE encompasses three critical components: (1) *body ownership*—feeling the surrogate as part of oneself; (2) *self-location*—a strong spatial telepresence at the remote site; and (3) *agency*—the confidence that one’s intentions directly produce corresponding actions in the remote environment. In many real-world applications—particularly industrial and field scenarios—the most relevant embodiment components are agency and self-location [13], which directly influence the operator’s control quality and task performance.

Thus, a strong SoE is crucial for successful teleoperation. When the SoE is strong, the operator no longer perceives the surrogate, the teleoperated robot, as an external tool, but rather as an extension of their own body and sensorimotor system [14]. This shift minimizes cognitive load and enhances the

This work is supported by Business Finland partnership project “Future all-electric rough terrain autonomous mobile manipulators” (Grant 2334/31/222). Corresponding author: Mahdi Hejrati

All authors are with the Department of Engineering and Natural Science, Tampere University, 7320 Tampere, Finland (e-mail: mahdi.hejrati@tuni.fi, pauli.mustalahti@tuni.fi, jouni.mattila@tuni.fi).

fluidity of task execution. Immersion is one key to evoking this SoE. Through the combination of visual feedback, delivered via a virtual reality (VR) headset, and distributed haptic feedback from force-reflective exoskeletons, immersive bilateral teleoperation creates more realistic task operation. But for immersion to truly support embodiment, it must be grounded in two essential pillars, each addressing relevant components of SoE: precise control, which reinforces the operator's sense of agency, and appropriate equipment, which anchors their sense of self-location. This study addresses both dimensions in the context of industrial surrogates, focusing on HHMs. By developing a robust, high-accuracy control framework and pairing it with immersive, well-integrated hardware, we aim to strengthen both agency and self-location. This enables HHMs to combine human-like precision with mechanical strength, empowering operators to perform complex tasks efficiently and safely in hazardous or unstructured environments.

## II. RELATED WORKS

### A. Sense of Self-Location

Immersive bilateral teleoperation relies on the integration of multi-modal sensory feedback, including visual, auditory, and haptic cues, to foster a stronger connection between the human operator and the remote environment. This immersive experience enhances the SoT, which in turn reinforces the sense of self-location (SoSL), as the two are closely inter-linked. It is important to note, however, that not all sensory inputs contribute equally to immersion. Visual feedback, in particular, plays a foundational role in shaping the immersive experience during teleoperation [15]. Yet, immersion itself is a qualitative and often comparative concept [11]; one system can be considered as more immersive than another with the given visual feedback, if, for instance, it provides real-time egocentric head-tracking compared to one with static camera. Even within the same system configuration, enhancements such as higher display resolution or the addition of haptic feedback can further elevate the sense of immersion, and, by extension, strengthen the operator's SoSL.

Building upon this foundation, Cheng et al. [16] introduced Open-TeleVision, an immersive teleoperation system that allows operators to intuitively perceive the robot's environment in a stereoscopic manner. Central to their approach is a stereo RGB camera mounted on the humanoid robot's head, equipped with a mechanism that dynamically tracks the operator's head movements. This configuration enables real-time, egocentric visual feedback streamed directly to a VR device, effectively strengthening the operator's sense of being present in the remote environment. Transitioning from single-view perception to a more comprehensive spatial awareness, [17] proposes a system for dual-arm bilateral teleoperation that further boosts the SoE. Their method combines multi-view visual feedback with haptic interaction, offering the operator five distinct visual sections—each from different camera perspectives—alongside real-time force graphs and parameter reconfiguration. This multi-faceted feedback setup allows the operator to maintain a heightened situational awareness, contributing to more precise and confident task execution. The immersive teleoperation

framework proposed in [18] increased the task execution performance by balancing the trade-off between data streaming costs and data visual quality in immersive VR. Other papers, moreover, leveraged the enhanced VR to achieve higher degrees of immersion in teleoperation [19], [20]. Expanding on the integration of sensory modalities, [21] presents a visual-haptic perception and reconstruction system designed to enhance telepresence. Their system not only delivers visual information from the remote site through VR but also provides haptic guidance to the operator, fostering a stronger cognitive and physical connection to the task environment.

Collectively, these works highlight a consistent theme: SoSL, mostly driven by synchronized visual feedback and enhanced with haptic cues, is pivotal for effective and high-performance teleoperation. As recent research continues to demonstrate, the more immersive and responsive the feedback, the stronger the operator's SoSL becomes, ultimately enabling more intuitive and accurate teleoperation.

### B. Sense of Agency

As the sense of agency (SoA) heavily rely on the trust of operator on that his/her actions will be mirrored by the surrogate, reinforcing this sense requires the design of adaptive and robust control algorithms capable of ensuring that the surrogate system accurately replicates human commands. From the perspective of control theory, accomplishment of such an objective relies on two criteria: *stability* and *transparency* [1] of the bilateral teleoperation system. The primary stability issue in bilateral teleoperation arises from time delays in the communication medium between the master and surrogate [22]. In addition, stability can be adversely affected by the system's interaction with both the human (active) and the environment (passive). Meanwhile, low transparency often stems from unknown uncertainties in the human/master and the surrogate/environment models. Though they may appear to be distinct objectives, stability and transparency are deeply interconnected. The central challenge in this field lies in achieving a high level of both, without compromising either [23]. Over the past few decades, extensive research has been conducted to address these objectives [24], [25]. Therefore, enhancing the SoA fundamentally depends on achieving stable and transparent bilateral teleoperation control. This necessitates the development of robust and high-performance control strategies that can guarantee reliable and intuitive operation.

Many advanced control methods have been developed for electric master-surrogate systems with similar configurations [26]–[29], where joint-to-joint mapping is employed to close the control loop, limiting the applicability of methods to surrogates with dissimilar configurations. Dissimilar lightweight systems, still human-scale, with differing configurations and workspaces have also been investigated in the literature [30]–[33]. For example, in [34], a Force Dimension Sigma 7 haptic device is employed to teleoperate a 7-DoF KUKA robots by designing passivity-based admittance control scheme in the presence of time delay. The dissimilarity, furthermore, in the sense of cooperative teleoperation with single master and multi or bimanual surrogate systems has also been widely examined

[35], [36]. However, these approaches remain confined to systems within the human scale—where actuation dynamics, inertia, and control constraints are comparatively tractable. In contrast, the bilateral teleoperation of beyond-human-scale systems, such as HHMs, presents fundamentally different challenges. These include strong nonlinearities, significant time delays, and extreme motion/force scaling, which introduce severe sensorimotor disruption and control instability. Despite their growing industrial relevance, HHMs have been largely neglected in the teleoperation literature. Most prior work either assumes linear system behavior [37] or is limited to 1-DoF experimental setups [38], [39], which are insufficient for the operational demands of real-world, high-DoF, nonlinear systems.

With increased attention to controlling hydraulically driven actuators using advanced control schemes and addressing accuracy and stability challenges, studies such as [40]–[43] have paved the way for achieving stable and high-fidelity bilateral teleoperation of hydraulic manipulators. In [44], [45], the bilateral teleoperation of 2-DoF HHMs with arbitrary motion-force scaling is examined, incorporating estimated human exogenous force and surrogate/environment interaction forces to ensure stability and transparency. To overcome the poor dynamics of HHMs, an integration of locally weighted intent prediction with a blended shared control method is proposed in [46]. Furthermore, [47] investigates the bilateral teleoperation of 2-DoF HHMs in contact with both physical and virtual environments. The operational inefficiency of asymmetric master and hydraulically actuated surrogate is addressed in [48] through a novel human-machine interface that enhances vision and incorporates auditory feedback.

Consequently, most existing work on bilateral teleoperation focuses on symmetric or dissimilar human-scale systems with low DoF and electrically actuated robots. In contrast, teleoperation of large, beyond-human-scale systems—particularly HHMs—poses distinct challenges that remain largely unaddressed. These include nonlinear dynamics, extreme motion and force scaling, increased cognitive load, and sensorimotor mismatches. Ensuring transparency and stability under such conditions requires dedicated investigation for real-world deployment.

### C. Aims and Contributions

Building on the previous discussion, this paper aims to significantly improve the accuracy and performance of bilateral teleoperation for large, heavy-duty robotic systems by enhancing immersion and reinforcing the operator’s SoE. As depicted in Fig. 1a, we integrate a head-tracked pan-tilt camera system mounted on the surrogate, which synchronizes in real time with the operator’s natural egocentric head movements. This two-DoF active vision, as shown in Fig. 1b, delivers immersive, first-person feedback that aligns with the operator’s viewpoint, reinforcing spatial presence and self-location [15]. Complementing the visual feedback, we employ ABLE, a 7-DoF haptic exoskeleton [49], to deliver rich proprioceptive input (Fig. 1c). This device distributes the scaled impedance of the surrogate along the operator’s arm and reflects its contact

with remote environment, further strengthening the physical and cognitive link between operator and surrogate. In parallel, we design a robust, high-accuracy control framework capable of stabilizing the complex human-in-the-loop system under model uncertainties, time delays, and input nonlinearities. By maintaining stable and responsive behavior, this control architecture strengthens the operator’s SoA, fostering trust, precision, and control throughout the task. Therefore, the unique contributions of this work can be summarized as follows:

- A VR-based visual feedback system with egocentric head-tracking capability is designed to deliver immersive, perspective-aligned visuals. The VR headset includes an eye-tracking feature that enables gaze-contingent resolution enhancement, increasing the level of immersion. To deepen the embodied experience, the haptic exoskeleton provides both contact force reflection and the distributed impedance of the surrogate. Together, these technologies reinforce the operator’s SoE during task execution in a highly dissimilar teleoperation setup.
- A novel control strategy is developed to ensure the stability and transparency of the force-reflective bilateral teleoperation system. It accounts for the human-robot augmented dynamics, unknown model uncertainties, input nonlinearities, and arbitrary time delays. By embedding an interaction force estimation module for both the human/master and surrogate/environment sides, the proposed controller is well-suited for real-world deployment on heavy-duty manipulators, enabling intuitive, stable operation while enhancing the operator’s SoA.
- The proposed framework is deployed on a real-world heavy-duty teleoperation setup. Extensive experiments are conducted to evaluate the system’s robustness, transparency, and accuracy in both free-motion and contact-rich scenarios. Additionally, user studies assess the system’s usability and its effectiveness in enhancing SoE during task performance.

Beyond improving task performance in challenging heavy-duty scenarios, the proposed system also serves as a rich platform for data collection and skill transfer. Its immersive, embodied setup is ideally suited for training learning-based models, including imitation learning, an area gaining traction particularly in the context of lightweight and humanoid systems [16], [50]. This work thus lays a foundational step toward the full automation of beyond-human-scale robotic systems, combining human expertise with machine capability in a scalable, data-driven manner.

The rest of the paper is organized as follows. Section III explains the mathematical preliminaries. Section IV and V elaborate on control design and stability analysis of master and surrogate systems, respectively. Section VI is dedicated to stability and transparency analysis of force-reflected bilateral teleoperation setup. The experimental results are provided in Section VII. Finally, Section VIII concludes this study.

### III. MATHEMATICAL PRELIMINARIES

In this section, the mathematical foundation of the controller is explained along with the lemmas and assumptions employed

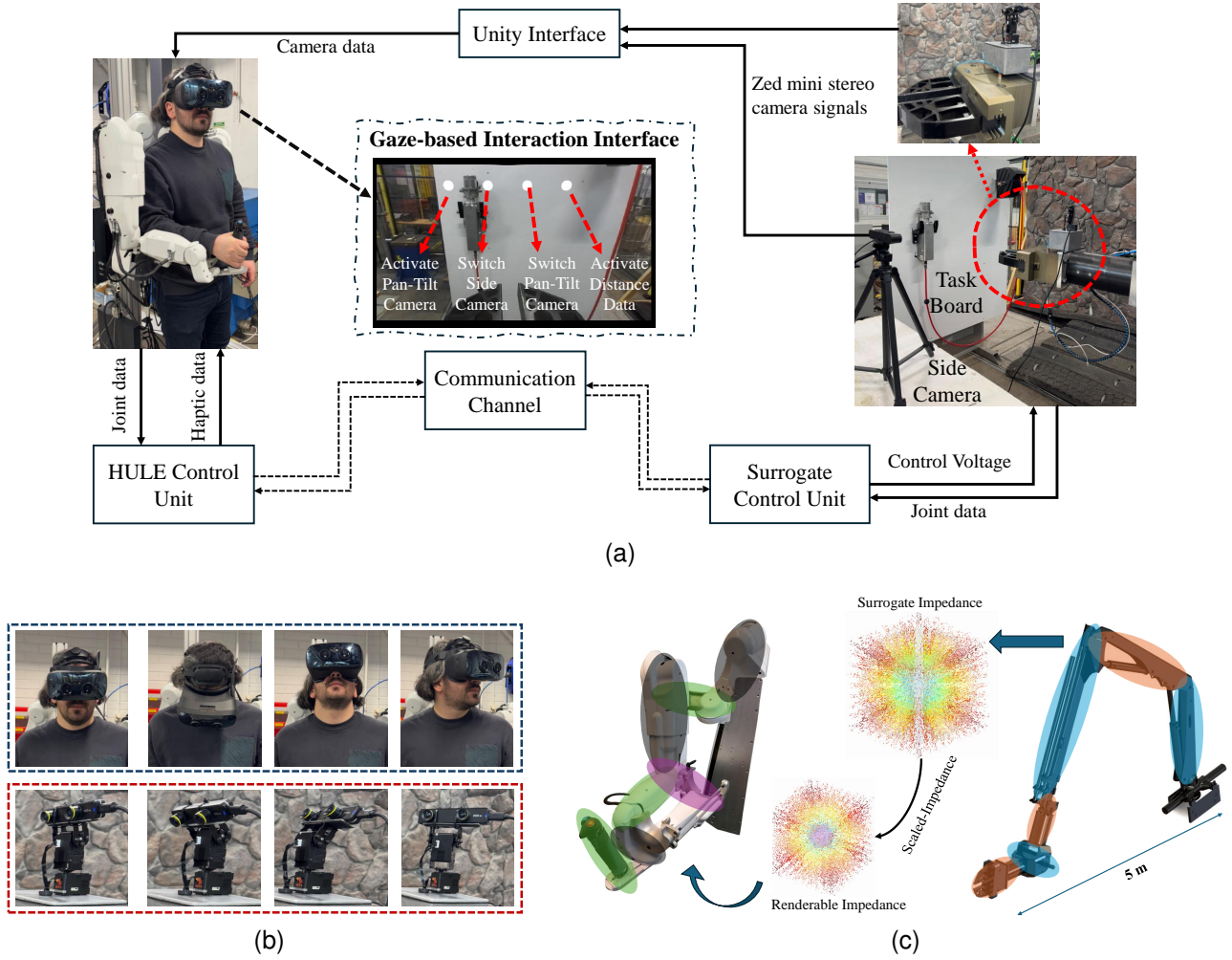


Fig. 1. Scheme of the VR-based immersive bilateral teleoperation system with egocentric head tracking system. (a) Overview of the general teleoperation framework, featuring control units, communication channels, and a gaze-based interaction interface. By utilizing the eye-tracking capability of the VR headset, the interface enables the operator to switch between modes based on gaze direction. The side camera further enhances situational awareness, especially in cases where the operator encounters difficulties during manipulation. (b) Pan-tilt mechanism of the remote camera, synchronized with the human operator's egocentric head movements to maintain intuitive visual feedback. (c) Visualization of the rendered and distributed scaled impedance of the surrogate onto the human operator's arm. The utilized haptic exoskeleton enables the operator to perceive both the dynamics of the surrogate and its interactions with the remote environment.

in the rest of the paper.

#### A. Virtual Decomposition Control

Virtual decomposition control (VDC) scheme is based on Plücker coordinate with compact formulation of system dynamics based on 6-D Plücker basis. In this coordinate system,  $\mathcal{M}^6$  denotes the space of spatial motions, while  $\mathcal{F}^6$  represents the space of spatial forces. Within these coordinates and spaces for a given frame  $\{A\}$  attached to a rigid body, the spatial velocity and force vectors can be defined as,

$${}^A V = [{}^A v, {}^A \omega]^T \in \mathcal{M}^6, \quad {}^A F = [{}^A f, {}^A \tau]^T \in \mathcal{F}^6$$

with  ${}^A v$ ,  ${}^A \omega$ ,  ${}^A f$ ,  ${}^A \tau$  being linear velocity, angular velocity, linear force, and moment, respectively, with respect to frame  $\{A\}$ . The spatial forces and velocity vectors can be transformed between frames as,

$${}^B V = {}^A U_B^T {}^A V, \quad {}^A F = {}^A U_B {}^B F \quad (1)$$

with  ${}^A U_B$  being transformation matrix between two frames, defined as,

$${}^A U_B = \begin{bmatrix} {}^A R_B & \mathbf{0}_{3 \times 3} \\ ({}^A r_{AB} \times) {}^A R_B & {}^A R_B \end{bmatrix} \quad (2)$$

where  ${}^A R_B \in \mathbb{R}^{3 \times 3}$  is a rotation matrix between frame  $\{A\}$  and  $\{B\}$ , and  $({}^A r_{AB} \times)$  is a skew-symmetric matrix operator defined as,

$${}^A r_{AB} \times = \begin{bmatrix} 0 & -r_z & r_y \\ r_z & 0 & -r_x \\ -r_y & r_x & 0 \end{bmatrix} \quad (3)$$

where  ${}^A r_{AB} = [r_x, r_y, r_z]^T$  denotes a vector from the origin of frame  $\{A\}$  to the origin of frame  $\{B\}$ , expressed in  $\{A\}$ .

VDC scheme decomposes the system into rigid body and joint subsystems, shown in Fig. 2, for each of which the modeling, control, and stability analysis are performed separately at each local subsystem. Then the local stability is extended to

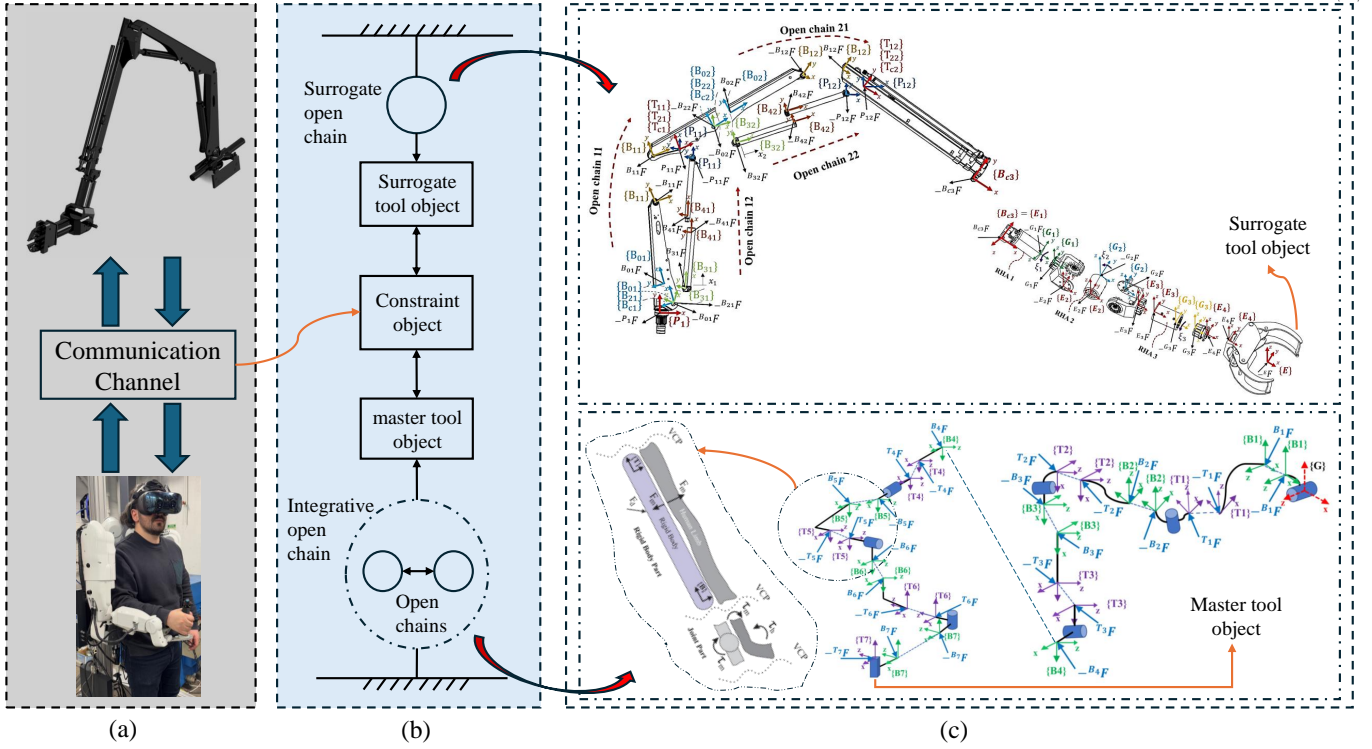


Fig. 2. Proposed control method for robust and transparent force-reflected bilateral teleoperation. (a) Schematic of an immersive bilateral teleoperation system. (b) Graph-based representation of the proposed teleoperation control strategy. Open chains represent serial robotic manipulators; the "object" denotes the connective constraint linking two open chains; and the integrative open chain models the interconnected structure of the exoskeleton's serial links and the human arm. (c) Virtual decomposition of the master and surrogate systems. The integrative open chain highlights how the augmented human–robot model is seamlessly incorporated into the control framework. Details regarding the decomposition of the master robot and surrogate system can be found in [51] and [52], respectively.

the stability of entire system by means of virtual power flow (VPF) and virtual stability. Within this context, the dynamics of the rigid body is independent of the system and is expressed in 6-D vector as,

$$M_A \frac{d}{dt}({}^A V) + C_A({}^A \omega) {}^A V + G_A(t) = {}^A F^* \quad (4)$$

with  $M_A \in \mathfrak{R}^{6 \times 6}$ ,  $C_A \in \mathfrak{R}^{6 \times 6}$ , and  $G_A \in \mathfrak{R}^6$  being spatial mass, centrifugal, gravitational matrices with  ${}^A F^* \in \mathfrak{R}^6$  being net spatial force applied to the rigid body [53], all defined in Plücker coordinates.

*Property 1:* [53] The rigid body dynamics in (4) can be written in linear-in-parameter form as,

$$M_A \frac{d}{dt}({}^A V) + C_A({}^A \omega) {}^A V + G_A(t) = \bar{Y}_A({}^A \dot{V}, {}^A V) \phi_A$$

with  $\bar{Y}_A({}^A \dot{V}, {}^A V) \in \mathfrak{R}^{6 \times 10}$  being regression matrix and  $\phi_A(m_A, h_A, I_A) \in \mathfrak{R}^{10}$  being known inertial parameter vector. Additionally,  $m_A$ ,  $h_A$ , and  $I_A$  are mass, first mass moment, and rotational inertia matrix, respectively.

*Definition 1:* [54] For the given frame  $\{A\}$ , the VPF is defined as the inner product of the spatial velocity vector error and the spatial force vector error,

$$p_A = ({}^A \mathcal{V}_r - {}^A \mathcal{V})^T ({}^A F_r - {}^A F).$$

where  ${}^A \mathcal{V}_r \in \mathcal{M}^6$  and  ${}^A F_r \in \mathcal{F}^6$  represent the required vectors of  ${}^A \mathcal{V} \in \mathcal{M}^6$  and  ${}^A F \in \mathcal{F}^6$ , respectively. The inner

product indicates the duality relationship between  $\mathcal{M}^6$  and  $\mathcal{F}^6$ .

*Definition 2:* A non-negative accompanying function  $\nu(t) \in \mathfrak{R}$  is a piecewise, differentiable function defined  $\forall t \in \mathfrak{R}^+$  with  $\nu(0) < \infty$  and  $\dot{\nu}(t)$  exists almost everywhere.

*Lemma 1:* [52] Consider a complex robot that is virtually decomposed into subsystems. Each subsystem is said to be virtually semi-globally uniformly ultimately bounded (SGUUB) with its non-negative accompanying function  $\nu(t)$  and its affiliated vector  $\dot{\nu}(t)$ , if and only if,

$$\dot{\nu} \leq -\alpha_1 \nu + \alpha_{10} + p_A - p_C \quad (5)$$

with  $\alpha_1$  and  $\alpha_{10}$  being positive constants and  $p_A$  and  $p_C$  denoting the sum of VPFs in the sense of Definition 1. This boundedness ensures robustness against unknown uncertainties, which is critical for real-world deployment.

Since the VDC is a velocity-based controller, the formulation of the required joint velocity plays a critical role. Its proper design enables the controller to handle a variety of tasks, such as free motion, in-contact interaction, and bilateral teleoperation. In this study, where the objective is to develop a controller for dissimilar bilateral teleoperation, the required end-effector velocities are first defined in (15) and (39). These velocities are then mapped to the corresponding joint space using the Jacobian matrices of the master and surrogate systems, resulting in the required joint velocities as shown in (16) and (40).

## B. Lemmas and Definitions

*Lemma 2:* Thanks to their universal approximation capability, radial basis function neural networks (RBFNNs) can be employed to estimate any given continues function  $\mathbf{f}(t)$  represented in frame  $\{A\}$  as,

$$\hat{\mathbf{f}}_A(t) = {}^A\hat{W}^T \psi(\chi_A) + {}^A\hat{\epsilon}$$

with  $\chi_A$  being the input vector,  ${}^A\hat{W}$  being the estimated weights,  $\psi(\cdot)$  being Gaussian basis function, and  ${}^A\hat{\epsilon}$  being estimation error of the RBFNNs. The adaptation laws for estimation of weights and bias of the network can be considered as follows [52],

$$\begin{aligned} {}^A\dot{\hat{W}} &= \Pi \left( \psi(\chi_A) ({}^A V_r - {}^A V)^T - \tau_0 {}^A \hat{W} \right) \\ {}^A\dot{\hat{\epsilon}} &= \pi \left( ({}^A V_r - {}^A V) - \pi_0 {}^A \hat{\epsilon} \right), \end{aligned}$$

where  $\Pi, \tau_0, \pi, \pi_0$  are positive constants. Under the optimal weights of RBFNNs as,

$$W^* = \arg \min_{\hat{W} \in \Xi_N} \left\{ \sup_{\chi \in \Xi_T} |\hat{\mathbf{f}}(\chi|\hat{W}) - \mathbf{f}(\chi)| \right\}$$

where  $\Xi_N = \{\hat{W} \mid \|\hat{W}\| \leq \kappa\}$  is a valid set of vectors with  $\kappa$  being a design value,  $\Xi_T$  is an allowable set of the state vectors, there is,

$$|\hat{\mathbf{f}}(\chi) - {}^A W^{*T} \psi(\chi_A)| = |\epsilon^*(\chi_A)| \leq \bar{\epsilon} \quad (6)$$

where  $\bar{\epsilon}$  is an unknown bound parameters.

*Lemma 3:* [55] Let  $k_b > 0$  be a positive constant, and define the sets  $\mathfrak{Z} := \{\mathfrak{z} \in \mathfrak{R} : -k_b < \mathfrak{z} < k_b\} \subset \mathfrak{R}$  and  $\mathcal{N} := \mathfrak{R}^l \times \mathfrak{Z} \subset \mathfrak{R}^{l+1}$ , which are open. Consider the dynamical system:

$$\dot{\eta} = \mathfrak{h}(t, \eta),$$

where  $\eta := [\omega, \mathfrak{z}]^T \in \mathcal{N}$ , and  $\mathfrak{h} : \mathfrak{R}_+ \times \mathcal{N} \rightarrow \mathfrak{R}^{l+1}$  is piecewise continuous in  $t$  and locally Lipschitz in  $\eta$ , uniformly in  $t$ , on  $\mathfrak{R}_+ \times \mathcal{N}$ . Suppose there exist functions  $\mathfrak{U} : \mathfrak{R}^l \rightarrow \mathfrak{R}_+$  and  $\mathfrak{V} : \mathfrak{Z} \rightarrow \mathfrak{R}_+$ , both continuously differentiable and positive definite in their respective domains, such that:

$$\mathfrak{V}(\mathfrak{z}) \rightarrow \infty \quad \text{as } \mathfrak{z} \rightarrow -k_b \quad \text{or } \mathfrak{z} \rightarrow k_b,$$

$$\delta_7(\|\omega\|) \leq \mathfrak{U}(\omega) \leq \delta_8(\|\omega\|),$$

where  $\delta_7$  and  $\delta_8$  are class  $\mathcal{K}_\infty$  functions. Let  $V(\eta) := \mathfrak{V}(\mathfrak{z}) + \mathfrak{U}(\omega)$ , and assume  $\mathfrak{z}(0) \in (-k_b, k_b)$ . If the following inequality holds:

$$\dot{V} = \frac{\partial V}{\partial \eta} \dot{\eta} \leq 0,$$

then  $\mathfrak{z}(t)$  remains in the open set  $(-k_b, k_b)$  for all  $t \in [0, \infty)$ .

*Definition 3:* For any unique representation of inertial parameter vector of rigid body  $\phi_A$ , there is one-to-one map as,

$$\mathcal{N}(\phi_A) = \mathcal{L}_A = \begin{bmatrix} 0.5tr(\bar{I})\mathbf{1} - I & h \\ h^T & m \end{bmatrix}$$

$$\mathcal{N}^{-1}(\mathcal{L}_A) = \phi_A(m, h, tr(\Sigma)\mathbf{1} - \Sigma)$$

where  $\Sigma = 0.5tr(I) - I$  and  $tr(\cdot)$  is the Trace operator of a matrix.

*Definition 4:* For a given  $\mathcal{L}_A$  with its estimation  $\hat{\mathcal{L}}_A$ , the natural adaptation law (NAL) can be derived as,

$$\dot{\hat{\mathcal{L}}}_A = \frac{1}{\gamma} \hat{\mathcal{L}}_A \left( \mathcal{S}_A - \gamma_0 \hat{\mathcal{L}}_A \right) \hat{\mathcal{L}}_A \quad (7)$$

with  $\gamma > 0$  being the adaptation gain for all the rigid bodies of the system, and  $\gamma_0 > 0$  being a small positive gain. Additionally,  $\mathcal{S}_A$  is a unique symmetric matrix defined in [51].

## C. Notation

In the remainder of the paper the following notation are used. For a given signal  $\mathbf{n}$ , the filtered signal  $\hat{\mathbf{n}}$  is computed as:

$$\dot{\hat{\mathbf{n}}} + \mathcal{C}\hat{\mathbf{n}} = \mathcal{C}\mathbf{n},$$

where  $\mathcal{C}$  is a positive constant for scalar signals and positive-definite matrix for vectors. The  $\hat{\mathbf{n}}$  represents the estimation of  $\mathbf{n}$  while  $\tilde{\mathbf{n}} = \hat{\mathbf{n}} - \mathbf{n}$ . The  ${}^A\mathbf{n}$  represents the signal defined in frame  $\{A\}$ .

## IV. AUGMENTED HUMAN/MASTER DYNAMICS AND CONTROL

The master robot utilized in this study is a 7-DoF haptic exoskeleton, shown in Fig. 3, which serves as both an exoskeleton and a haptic display. The objective of this section is to design a control action that not only renders the scaled impedance of the surrogate and its interaction with the environment, but also guarantees the safety of the human in the loop. The details of the controller design are presented in the following.

The decentralized human-robot augmented model, shown in Fig. 2c, proposed by [51] can be written as follows,

$$\mathcal{M}_B \frac{d}{dt} ({}^{B_i} \mathcal{V}) + \mathcal{C}_{B_i} {}^{B_i} \mathcal{V} + \mathcal{G}_{B_i} = {}^{B_i} \mathcal{F}^* - \Delta_{D_i} \quad (8)$$

$$\mathcal{I}_i \ddot{q}_i = \tau_i^* - \tau_{h_i} - \Delta_J \quad (9)$$

$$\tau_i = \tau_i^* + \tau_{ai} \quad (10)$$

where  $\mathcal{M}_B = M_r + M_h \in \mathfrak{R}^{6 \times 6}$ ,  $\mathcal{C}_B = C_r + C_h \in \mathfrak{R}^{6 \times 6}$ , and  $\mathcal{G}_B = G_r + G_h \in \mathfrak{R}^{6 \times 6}$  are augmented matrices in the form of (4),  $\mathcal{I} = I_r + I_h \in \mathfrak{R}^6$  being augmented rotational inertia of the joint,  $\tau_h$  being exogenous human torque (EHT),  $\Delta_D \in \mathfrak{R}^6$  and  $\Delta_J \mathfrak{R}^6$  encompassing unmodeled dynamics and compound input nonlinearity for rigid body and joint subsystems, respectively, with  $(\cdot)_r$  standing for robot and  $(\cdot)_h$  representing human-related terms

*Remark 1:* Equation (10) presents the recomposed dynamics of the decomposed system. The first term on the right-hand side of (10) represents the torque responsible for generating joint-level actions, while the second term,  $\tau_{ai} = \sigma^T {}^{B_i} \mathcal{F}$  where  ${}^{B_i} \mathcal{F}$  defined in (13), corresponds to the forces arising from the motion of the rigid body. It worth to note that the screw vector  $\sigma$  maps the spatial force  ${}^{B_i} \mathcal{F}$  from spatial forces space to the joint space.

Being grounded in the Newton-Euler recursive method, VDC necessitates the computation of forward spatial velocity and acceleration, as well as backward spatial force propagation. These steps are fundamental for designing the control law in Plücker coordinates. In the following, the computation process is detailed for the 7-DoF haptic exoskeleton.

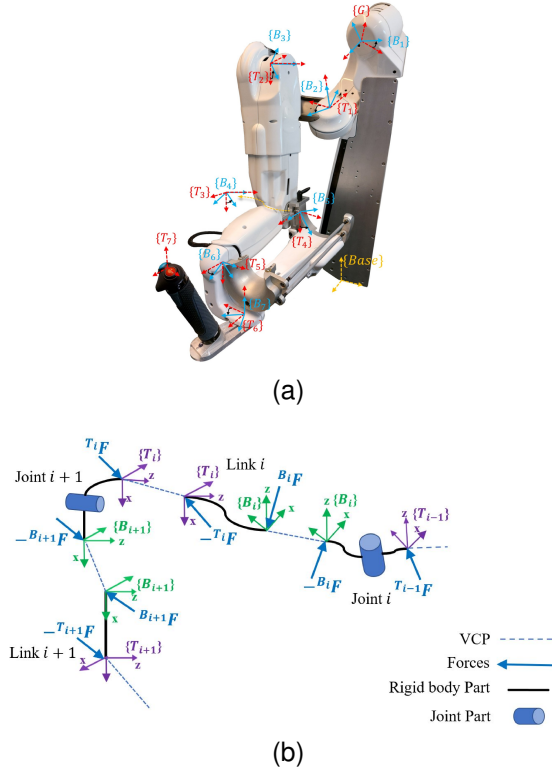


Fig. 3. Decomposition of haptic exoskeleton using the VCP concept. a) Framing convention in VDC context, b)  $i^{th}$  subsystem of decomposed model

1) *Kinematics and Dynamics*: Considering the framing convention depicted in Fig. 3a, the spatial velocity vectors for the  $i$ -th link of the decentralized system can be derived starting from the base frame as follows:

$${}^{B_i} \mathcal{V} = {}^{T_{i-1}} U_{B_i}^T {}^{T_{i-1}} \mathcal{V} + \sigma_i \dot{q}_i, \quad (11)$$

$${}^{T_i} \mathcal{V} = B_i U_{T_i}^T B_i \mathcal{V}, \quad (12)$$

for  $i = 1, \dots, 7$ , with  $\dot{q}_i$  being joint angular velocity. Once the spatial velocity and, consequently, the spatial acceleration are computed, the spatial forces can be determined as follows:

$$B_j \mathcal{F} = B_j U_{T_j}^T T_j \mathcal{F} + B_j \mathcal{F}^*, \quad (13)$$

$$T_{j-1} \mathcal{F} = T_{j-1} U_{B_j}^T B_j \mathcal{F}, \quad (14)$$

for  $j = 7, \dots, 1$ , where  $B_j \mathcal{F}^*$  represents the net spatial force applied to frame  $\{B\}$  as defined in (8). Fig. 3b illustrates the frames and spatial forces applied to the  $i^{th}$  decomposed subsystem. With the dynamics defined in (8)–(14), the corresponding control action can now be designed, as explained in the following sections.

2) *Control design*: In order to establish the force-reflected bilateral teleoperation, the required end-effector velocity of master robot can be defined as,

$$V_{mr} = V_{md} - \mathcal{A} F_m. \quad (15)$$

where  $V_{md} \in \mathbb{R}^6$  is defined in (56), and  $F_m \in \mathbb{R}^6$  denotes the estimated interaction force inserted from exoskeleton to the human arm, computed using the method proposed in [56]. Then,

using the pseudo-inverse of Jacobian matrix  $\mathcal{J}_m \in \mathbb{R}^{6 \times 7}$ , the joint level required velocity can be derived as,

$$\dot{q}_r = \mathcal{J}_m^\dagger V_{mr}. \quad (16)$$

The velocity term in (16) represents the motion that must be generated by the actuators of the master robot to fulfill the objectives of teleoperation. With this notion, the required spatial velocity of the rigid bodies can be computed by substituting (16) into (11)–(12) as follows:

$$B_i \mathcal{V}_r = {}^{T_{i-1}} U_{B_i}^T {}^{T_{i-1}} \mathcal{V}_r + \sigma_i \dot{q}_{ri} \quad (17)$$

$${}^{T_i} \mathcal{V}_r = B_i U_{T_i}^T B_i \mathcal{V}_r. \quad (18)$$

In the context of VDC, the forces that generate the required spatial velocities are referred to as required spatial forces. These forces correspond to those that would produce the required velocity described in (17) if applied to the rigid body. Consequently, the required spatial forces can be expressed as follows:

$$B_j \mathcal{F}_r = B_j U_{T_j}^T T_j \mathcal{F}_r + B_j \mathcal{F}_r^* \quad (19)$$

$$T_{j-1} \mathcal{F}_r = T_{j-1} U_{B_j}^T B_j \mathcal{F}_r. \quad (20)$$

with  $B_j \mathcal{F}_r^*$  being the required net spatial force of the rigid body defined in (22). Finally, the unified required joint torque can be computed in the sense of (10) as,

$$\tau_{ri} = \tau_{ri}^* + \tau_{ari} \quad (21)$$

with  $\tau_{ari} = \sigma_i^T B_i \mathcal{F}_r$ , and  $\tau_{ri}^*$  defined in (23). Addressing the unknown uncertainties and dynamics of the rigid bodies and joints, the control signal in (21) achieves the objectives of the teleoperation system by generating the required joint velocity described in (16).

*Theorem 1*: For the decentralized and augmented model of pHRI described in (8)–(10), along with the spatial velocity and force computations in (11)–(14) and (17)–(20), the decentralized control actions can be designed as follows:

$$B_i \mathcal{F}_r^* = \mathcal{K}_{Di} (B_i \mathcal{V}_r - B_i \mathcal{V}) + \hat{W}_{Di}^T \Psi(\chi_{Di}) + \hat{\epsilon}_{Di} + Y_{B_i} \hat{\phi}_{B_i} \quad (22)$$

$$\tau_{ri}^* = k_{di} (\dot{q}_{ri} - \dot{q}_i) + Y_{ai} \hat{\phi}_{ai} + \hat{W}_{Ji}^T \Psi(\chi_{Ji}) + \hat{\epsilon}_{Ji} + \frac{e_{ai} + c_1 \dot{e}_{ai}^2}{k_{bi}^2 - e_{ai}^2} \quad (23)$$

which ensures the SGUUB of all signals in the closed loop system. Additionally, the followings hold,

$$e_{ai} \in \Omega_e, \quad (24)$$

$$\rho_m \stackrel{\text{def}}{=} V_{mr} - V_m = V_{md} - V_m - \mathcal{A} F_m \in \Omega_m, \quad (25)$$

$$\Omega_m \stackrel{\text{def}}{=} \{V_{mr} - V_m \in \mathbb{R}^6 \mid \|V_{mr} - V_m\| \leq \mathcal{D}_m\} \quad (26)$$

$$\Omega_e \stackrel{\text{def}}{=} \{e_{ai} \in \mathbb{R} \mid |q_{ri} - q_i| \leq \mathcal{D}_1, \|\dot{q}_{ri} - \dot{q}_i\| \leq \mathcal{D}_2\}. \quad (27)$$

*Proof 1*: Defining non-negative accompanying function as,

$$v_m(t) = \sum_{i=1}^7 (v_i(t) + v_{ai}(t)) \quad (28)$$

$$\begin{aligned} \nu_i(t) &= \frac{1}{2}({}^{B_i}\mathcal{V}_r - {}^{B_i}\mathcal{V})^T \mathcal{M}_{B_i} ({}^{B_i}\mathcal{V}_r - {}^{B_i}\mathcal{V}) \\ &+ \gamma_1 \mathcal{D}_F(\mathcal{L}_{B_i} \|\hat{\mathcal{L}}_{B_i}) + \frac{1}{2} \text{tr}(\tilde{W}_{D_i}^T \Gamma_{B_i}^{-1} \tilde{W}_{D_i}) \\ &+ \frac{1}{2\gamma_{2i}} \tilde{\varepsilon}_{D_i}^T \tilde{\varepsilon}_{D_i}. \end{aligned} \quad (29)$$

$$\begin{aligned} \nu_{ai}(t) &= \frac{1}{2} \mathcal{I}_i (\dot{q}_{ri} - \dot{q}_i)^2 + \frac{1}{2} \log \frac{k_{bi}^2}{k_{bi}^2 - e_{ai}^2} \\ &+ \zeta \mathcal{D}_F(\mathcal{L}_{ai} \|\hat{\mathcal{L}}_{ai}) + \frac{1}{2\beta_{2i}} \tilde{\varepsilon}_{J_i}^2 + \frac{1}{2\beta_{1i}} \tilde{W}_{J_i}^T \tilde{W}_{J_i} \end{aligned} \quad (30)$$

and taking its time derivative, replacing adaptation functions from Lemma 2 and (7), the local controllers in (22) and (23) along with employing Young's inequality as  $-\text{tr}(\hat{\mathcal{L}}_{B_i} \tilde{\mathcal{L}}_{B_i}) \leq -0.5 \text{tr}(\tilde{\mathcal{L}}_{B_i} \tilde{\mathcal{L}}_{B_i}) + 0.5 \text{tr}(\mathcal{L}_{B_i} \mathcal{L}_{B_i})$ ,  $-\text{tr}(\tilde{W}_{D_i}^T \tilde{W}_{D_i}) \leq -0.5 \text{tr}(\tilde{W}_{D_i}^T \tilde{W}_{D_i}) + 0.5 \text{tr}(W_{D_i}^T W_{D_i})$ ,  $-\tilde{\varepsilon}_{D_i}^T \tilde{\varepsilon}_{D_i} \leq -0.5 \tilde{\varepsilon}_{D_i}^T \tilde{\varepsilon}_{D_i} + 0.5 \varepsilon_{D_i}^T \varepsilon_{D_i}$ ,  $-\tilde{\varepsilon}_{J_i}^T \tilde{\varepsilon}_{J_i} \leq -0.5 \tilde{\varepsilon}_{J_i}^T \tilde{\varepsilon}_{J_i} + 0.5 \varepsilon_{J_i}^T \varepsilon_{J_i}$ , we have,

$$\begin{aligned} \dot{\nu}_m(t) &\leq - \sum_{i=1}^n [({}^{B_i}\mathcal{V}_r - {}^{B_i}\mathcal{V})^T \mathcal{K}_{D_i} ({}^{B_i}\mathcal{V}_r - {}^{B_i}\mathcal{V}) \\ &+ k_{di} (\dot{q}_{ri} - \dot{q}_i)^2 + 0.5 \gamma_{0m} \text{tr}(\tilde{\mathcal{L}}_{B_i} \tilde{\mathcal{L}}_{B_i}) \\ &+ 0.5 \tau_{0m} \text{tr}(\tilde{W}_{D_i}^T \tilde{W}_{D_i}) + \pi_{0m} \tilde{\varepsilon}_{D_i}^T \tilde{\varepsilon}_{D_i} + \pi_{0m} \tilde{\varepsilon}_{J_i}^T \tilde{\varepsilon}_{J_i} \\ &+ 0.5 \gamma_{0m} \text{tr}(\tilde{\mathcal{L}}_{ai} \tilde{\mathcal{L}}_{ai}) + 0.5 \tau_{0m} \text{tr}(\tilde{W}_{J_i}^T \tilde{W}_{J_i}) \\ &+ c_1 \frac{e_{ai}^2}{k_{bi}^2 - e_{ai}^2}] + \sum_{i=1}^n [0.5 \gamma_{0m} \text{tr}(\mathcal{L}_{B_i} \mathcal{L}_{B_i}) \\ &+ 0.5 \tau_{0m} \text{tr}(W_{D_i}^T W_{D_i}) + \pi_{0m} \varepsilon_{D_i}^T \varepsilon_{D_i} + \pi_{0m} \varepsilon_{J_i}^T \varepsilon_{J_i} \\ &+ 0.5 \gamma_{0m} \text{tr}(\mathcal{L}_{ai} \mathcal{L}_{ai}) + 0.5 \tau_{0m} \text{tr}(W_{J_i}^T W_{J_i})] \\ &\leq -\vartheta \nu_m(t) + \vartheta_0 - p_{T_7} \end{aligned} \quad (31)$$

where  $\vartheta_0 = 0.5 \gamma_{0m} \text{tr}(\mathcal{L}_{B_i} \mathcal{L}_{B_i}) + 0.5 \tau_{0m} \text{tr}(W_{D_i} W_{D_i}) + \pi_{0m} \varepsilon_{D_i} \varepsilon_{D_i} + \pi_{0m} \varepsilon_{J_i} \varepsilon_{J_i} + 0.5 \gamma_{0m} \text{tr}(\mathcal{L}_{ai} \mathcal{L}_{ai}) + 0.5 \tau_{0m} \text{tr}(W_{J_i} W_{J_i})$ , and  $\vartheta = \vartheta_{min}/\vartheta_{max}$ , with  $\vartheta_{min} = \min(\min(k_{di}), \min(\mathcal{K}_{D_i}), \gamma_{0m}, \tau_{0m}, c_1, \pi_{0m})$  and,

$$\begin{aligned} \vartheta_{max} &= \max(\max(M_{B_i}), \max(\mathcal{K}_{D_i}), \gamma_{1m}, \max(\Gamma_{B_i}), \\ &\max(\gamma_{2i}^{-1}), \max(\mathcal{I}_i), \max(\beta_{2i}^{-1}), \max(\beta_{1i}^{-1}), \zeta, 1), \end{aligned} \quad (32)$$

where the following inequality is used,

$$\log \frac{k_{bi}^2}{k_{bi}^2 - e_{ai}^2} \leq \frac{e_{ai}^2}{k_{bi}^2 - e_{ai}^2}, \quad (33)$$

According to (31) all the VPFs cancel out each other as shown in Appendix B of [51] except  $p_{T_7}$ , which indicates the virtual power flow between human hand and the robot. Then, by integrating both side of (31), one can obtain,

$$\nu_m(t) \leq \nu(0) e^{-\vartheta t} + \frac{\vartheta_0}{\vartheta} (1 - e^{-\vartheta t}) + \varrho_m. \quad (34)$$

with  $\varrho_m$  defined in Appendix A. According to (34) and Appendix A, the maximum and steady-state value of  $\nu_m$  can be derived as,  $\nu_m(t) \leq \nu_{max} = \nu(0) + \vartheta_0/\vartheta + \varrho_m$  and  $\lim_{t \rightarrow \infty} \nu_m(t) \leq \vartheta_0/\vartheta + \varrho_{0m}$ , with  $\varrho_{0m}$  defined in Appendix A. Then, the following holds from (28),

$$\frac{1}{2} \log \frac{k_{bi}^2}{k_{bi}^2 - e_{ai}^2} \leq \nu_m(t) \leq \nu_{max}. \quad (35)$$

Taking the exponential on both sides of (35) and rearranging the terms, we can show that,

$$|e_{ai}| \leq k_{bi} \sqrt{1 - e^{-2\nu_{max}}} = \mathcal{D}_1. \quad (36)$$

In the same way, it can be shown that,

$$\|\dot{q}_{ri} - \dot{q}_i\| \leq \sqrt{\frac{2\nu_{max}}{\lambda_{min}(\mathcal{I}_i)}} = \mathcal{D}_2 \quad (37)$$

$$\|V_{mr} - V_m\| \leq \alpha_m \sqrt{\frac{2\nu_{max}}{\lambda_{min}(M_{B_7})}} = \mathcal{D}_m. \quad (38)$$

with  $\|{}^{B_7}U_{T_7}\| \leq \alpha_m$ . Additionally, considering Lemma 3 and (34), we have  $|e_{ai}| \leq k_{bi}$ . Then from  $q_i = q_{ri} - e_{ai}$  and  $|q_{ri}| \leq k_{ri}$ , we can conclude that  $|q_i| \leq k_{ci} = k_{ri} + k_{bi}$  if  $e_{ai}(0) \leq k_{bi}$ , ensuring that state-constraints will not be violated.

## V. SURROGATE/ENVIRONMENT DYNAMICS AND CONTROL

The surrogate in this study is a 6-DoF HHM with a 3-DoF anthropomorphic arm and a spherical wrist, shown in Fig. 4, encompassing the complexities arising from fluid dynamics and the nonlinearities of a high-DoF system. The primary objective of the surrogate is to accurately follow the motion and force commands from the master robot while ensuring stable contact with an unknown environment. Furthermore, since the use of force sensors in HHMs is not always a feasible solution, a force-sensorless control law is designed to address this issue effectively.

For doing so, the required end-effector velocity of the surrogate can be defined as,

$$V_{sr} = V_{sd} - \mathbf{A} \mathbf{F}_s \quad (39)$$

with  $V_{sd} \in \mathbb{R}^6$  defined in (57) and  $\mathbf{F}_s \in \mathbb{R}^6$  denotes the estimated interaction force between surrogate end-effector and remote environment, computed using the method proposed in [56]. Then, using the damped least square (DLS) inverse of Jacobian matrix  $\mathcal{J}_s \in \mathbb{R}^{6 \times 6}$ , one can obtain the required joint velocity as follows,

$$\dot{\theta}_r = \{(\mathcal{J}_s^T \mathcal{J}_s + \lambda I)^{-1} \mathcal{J}_s^T\} V_{sr} \quad (40)$$

with  $\lambda \in \mathcal{R}$  being damping factor. The use of DLS method tackles the gimbal lock effect, which is a common phenomenon in spherical wrists. To enhance readability and avoid redundancy, only the tool of the surrogate is considered to demonstrate the control design in this study. The comprehensive analysis of the entire system, for both free-motion and in-contact tasks, is elaborated in [52] and [56]. Therefore, as shown in Fig. 4, it is assumed that the velocity computations and force backpropagations are performed up to frame  $\{G_3\}$  for both  $\dot{\theta}$  and  $\dot{\theta}_r$  in (40), as described in [52].

At the time of contact, the following hold

$${}^T F = N_e f_e \quad (41)$$

where,

$$f_e = M_e \dot{V}_s + D_e V_s + K_e x_e \quad (42)$$

with  $x_e$  being the deformation of the environment,  $M_e$ ,  $D_e$ , and  $K_e$  being the environmental mass, damping, and stiffness

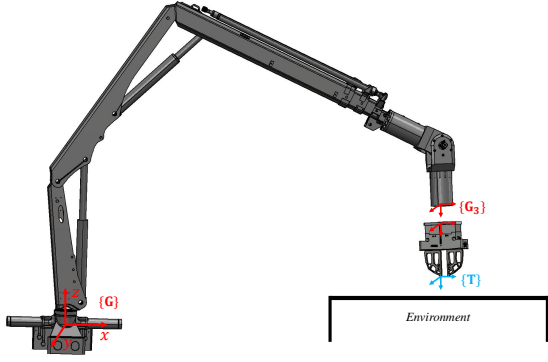


Fig. 4. Scheme of 6-DoF HMM in presence of unknown environment

matrices, respectively. Therefore, the force resultant on the tool body can be written,

$${}^{G_3}F^* = {}^{G_3}F - {}^{G_3}U_T^T F, \quad (43)$$

where, the net spatial force vector  ${}^{G_3}F^*$  of the tool can be written in the sense of (4) as,

$$M_{G_3} \frac{d}{dt} ({}^{G_3}V) + C_{G_3} ({}^{G_3}\omega) {}^{G_3}V + G_{G_3} + {}^{G_3}\Delta_R(t) = {}^{G_3}F^*. \quad (44)$$

with  $\Delta_R(t)$  being unknown uncertainty. Considering (40), the following hold,

$${}^{G_3}V_r = {}^T U_{G_3}^T {}^T V_r, \quad (45)$$

$${}^T F_r = N_c f_{ed}, \quad (46)$$

$${}^{G_3}F_r^* = Y_{G_3} \hat{\phi}_{G_3} + K_{G_3} ({}^{G_3}V_r - {}^{G_3}V) + {}^{G_3}\hat{\Delta}_R, \quad (47)$$

$$f_{ed} = M_e \dot{V}_{sr} + D_e V_s + K_e x_e. \quad (48)$$

where  ${}^{G_3}\hat{\Delta}_R$  is in the sense of Lemma 2. According to (43), the required spatial force vector, which acts as the control signal for tool body, can be written as,

$${}^{G_3}F_r = {}^{G_3}F_r^* + {}^{G_3}U_T^T F_r. \quad (49)$$

Consequently, the required piston force can be computed as,

$$f_{cr} = \frac{1}{r_w} \sigma^T {}^{G_3}F_r + \sigma^T G_{p3} F_r^* \quad (50)$$

where  $r_w$  being gear ratio of helical gears in the actuator and  ${}^{G_{p3}}F_r^*$  being the net required spatial force of piston body in the sense of (47).

*Remark 2:* The first term in (50) accounts for the dynamics of the rigid body subsystem, while the second term compensates for the joint mechanism's dynamics and uncertainties, ensuring the fulfillment of the control objectives. The low-level voltage control for generating the required piston force follows the approach outlined in [52].

*Theorem 2:* The tool of the surrogate with dynamics represented in (44) and required net spatial force defined in (47) is virtually SGUUB.

*Proof 2:* Following the same procedure in [56, Theorem 2] for frame  $\{G_3\}$  with non-negative accompanying function  $\nu_{G_3}$ , the following holds,

$$\dot{\nu}_{G_3} \leq -\mu \nu_{G_3} + \mu_0 + p_{G_3} - p_T \quad (51)$$

with  $\mu$  and  $\mu_0$  being positive constants,  $p_{G_3}$  being VPF of driving cutting point, and  $p_T$  is the VPF between surrogate end-effector and environment. According to Lemma 1 and (51), the tool subsystem is virtually SGUUB.

When there is no contact with the environment,  $p_T = 0$ . However, during contact,  $p_T$  represents the power flow between the surrogate and the remote environment. The following lemma used to tackle  $p_T$  during contact.

*Lemma 4:* The following holds for  $p_T$ ,

$$\lim_{t \rightarrow \infty} \int_0^t p_T dt \geq -\varrho_{0s} \quad (52)$$

where  $\varrho_{0s}$  is a positive constant.

*Proof 3:* Appendix B.

*Theorem 3:* Consider the surrogate decomposed into subsystems employing VCP concept. Then, for all  $\mathbf{A} \in \Psi$ , where  $\Psi$  encompasses all the rigid body frames attached to the subsystem except  $\{G_3\}$ , with,

$$\nu_s = \nu_{G_3} + \sum_{\mathbf{A} \in S} \nu_{\mathbf{A}} + \sum_{j=1,6} (f_{pjr} - f_{pj})^2 / (2\beta k_{xj}). \quad (53)$$

all the signals of the closed-loop system are SGUUB. Consequently, the following holds,

$$\rho_s \stackrel{\text{def}}{=} V_{sr} - V_s = V_{sd} - V_s - \mathcal{A}F_s \in \Omega_s. \quad (54)$$

where

$$\Omega_s \stackrel{\text{def}}{=} \{V_{sr} - V_s \in \mathbb{R}^6 \mid \|V_{sr} - V_s\| \leq \alpha \sqrt{\frac{2(\bar{\mu}_0 + \varrho_s)}{\lambda_{\min}(M_{G_3})\bar{\mu}}}\}. \quad (55)$$

where  $\|{}^{G_3}U_T^T\| \leq \alpha_s$ ,  $\|p_T\| \geq \varrho_s$  with  $\bar{\mu}$  and  $\bar{\mu}_0$  being positive constants.

*Proof 4:* The proof follows the same approach as outlined in [52, Theorem 3] and Theorem 1, using Lemma 4.

## VI. DISSIMILAR BILATERAL TELEOPERATION

In this section, the desired master and surrogate velocities, denoted as  $V_{md}$  and  $V_{sd}$ , are designed to enable dissimilar bilateral teleoperation through the communication channel with motion/force scaling. To achieve this, we define:

$$V_{md} = \kappa_p^{-1} (V_s + \Lambda [X_s - \kappa_p X_m] - \mathcal{A} [F_s + (\kappa_f - \kappa_p) F_m]), \quad (56)$$

$$V_{sd} = \kappa_p (V_m + \Lambda X_m) - \Lambda X_s - \mathcal{A} \kappa_f F_m, \quad (57)$$

where  $\kappa_p \in \mathcal{R}^{6 \times 6}$  and  $\kappa_f \in \mathcal{R}^{6 \times 6}$  are the motion and force scaling matrices, respectively;  $\Lambda \in \mathcal{R}^{6 \times 6}$  is a positive-definite matrix; and  $X_m$ ,  $V_m$ ,  $X_s$ , and  $V_s$  represent the pose and velocity of the master robot and the pose and velocity of the surrogate end-effectors, respectively. As can be seen, the designed velocity commands not only incorporate motion and force scaling, but also enable both force reflection and force tracking. It is important to note that, in this study, orientation error is computed based on quaternions.

### A. Stability Analysis

1) *Stability without delay*: Substituting (56) and (57) into (25) and (54), respectively, with  $\dot{X}_m = V_m$  and  $\dot{X}_s = V_s$ , we can write,

$$\begin{aligned} \rho_s - \kappa_p \rho_m &= \kappa_p \mathbf{V}_m - \mathbf{V}_s + \Lambda[\kappa_p \mathbf{X}_m - \mathbf{X}_s] + \kappa_p V_m \\ &\quad - V_s + \Lambda[\kappa_p X_m - X_s] \\ &= \mathbf{e} + e \end{aligned} \quad (58)$$

with,

$$e \stackrel{\text{def}}{=} \kappa_p V_m - V_s + \Lambda[\kappa_p X_m - X_s]. \quad (59)$$

According to results of Theorem 1 and 3 along with (58), one can obtain,

$$e \in \Omega_T \quad (60)$$

$$\Omega_T \stackrel{\text{def}}{=} \{e \in \mathbb{R}^6 \mid \|e\| \leq \alpha_s \sqrt{\frac{2(\bar{\mu}_0 + \varrho_s)}{\lambda_{\min}(M_{G_3})\bar{\mu}}} + \kappa_p \mathcal{D}_m\} \quad (61)$$

leading to,

$$\rho_v \stackrel{\text{def}}{=} \kappa_p V_m - V_s \in \Omega_T \quad (62)$$

$$\rho_p \stackrel{\text{def}}{=} \kappa_p X_m - X_s \in \Omega_T. \quad (63)$$

The above equations ensure the boundedness of velocity and position errors during both free-motion and in-contact phases of teleoperation in the presence of unknown uncertainties, human exogenous forces, and environmental forces.

2) *Stability with delay*: In order to address time delays existing in communication medium between master and surrogate, the expressions in (56) and (57) can be modified as,

$$\begin{aligned} V_{md} &= \kappa_p^{-1}(e^{-s\mathcal{T}}(\mathbf{V}_s + \Lambda \mathbf{X}_s) - \kappa_p \Lambda X_m \\ &\quad - \mathcal{A}[e^{-s\mathcal{T}} \mathbf{F}_s + (\kappa_f - \kappa_p) \mathbf{F}_m]) \end{aligned} \quad (64)$$

$$V_{sd} = e^{-s\mathcal{T}} \kappa_p (\mathbf{V}_m + \Lambda \mathbf{X}_m) - \Lambda X_s - e^{-s\mathcal{T}} \mathcal{A} \kappa_f \mathbf{F}_m \quad (65)$$

with  $\mathcal{T}$  being one-way arbitrary time delay. Substituting (64) and (65) in (25) and (54), one can obtain,

$$\begin{aligned} \kappa_p (\mathbf{V}_m + \Lambda \mathbf{X}_m) + \mathcal{A} \kappa_f \mathbf{F}_m &= e^{-s\mathcal{T}} [\mathbf{V}_s + \Lambda \mathbf{X}_s \\ &\quad - \mathcal{A} \mathbf{F}_s] - \kappa_p \rho_m \end{aligned} \quad (66)$$

$$\begin{aligned} \mathbf{V}_s + \Lambda \mathbf{X}_s + \mathbf{A} \mathbf{F}_s &= e^{-s\mathcal{T}} [\kappa_p (\mathbf{V}_m + \Lambda \mathbf{X}_m) \\ &\quad - \mathcal{A} \kappa_f \mathbf{F}_m] - \rho_s. \end{aligned} \quad (67)$$

Then, the stability of the teleoperation system under arbitrary time delay  $\mathcal{T} > 0$  can be ensured by satisfying the following sufficient condition,

$$\begin{cases} \|\mathcal{H}_{1s}(j\omega)^{-1} \mathcal{H}_{2s}(j\omega) \mathcal{H}_{1m}(j\omega)^{-1} \mathcal{H}_{2m}(j\omega)\|_\infty < 1, \\ \|\mathcal{H}_{1m}(j\omega)^{-1} \mathcal{H}_{2m}(j\omega) \mathcal{H}_{1s}(j\omega)^{-1} \mathcal{H}_{2s}(j\omega)\|_\infty < 1 \end{cases} \quad (68)$$

with,

$$\mathcal{H}_{1s}(s) \stackrel{\text{def}}{=} (s\mathbf{I} + \Lambda)(\mathcal{C}^{-1}s + \mathbf{I}_6) + s\mathbf{A}\mathbf{Z}_e(s) \quad (69)$$

$$\mathcal{H}_{2s}(s) \stackrel{\text{def}}{=} (s\mathbf{I} + \Lambda)\mathbf{I}_6 - s\mathcal{A}\kappa_f\kappa_p^{-1}\mathbf{Z}_h(s) \quad (70)$$

$$\mathcal{H}_{1m}(s) \stackrel{\text{def}}{=} (s\mathbf{I} + \Lambda)(\mathcal{C}^{-1}s + \mathbf{I}) + s\mathcal{A}\kappa_f\kappa_p^{-1}\mathbf{Z}_h(s) \quad (71)$$

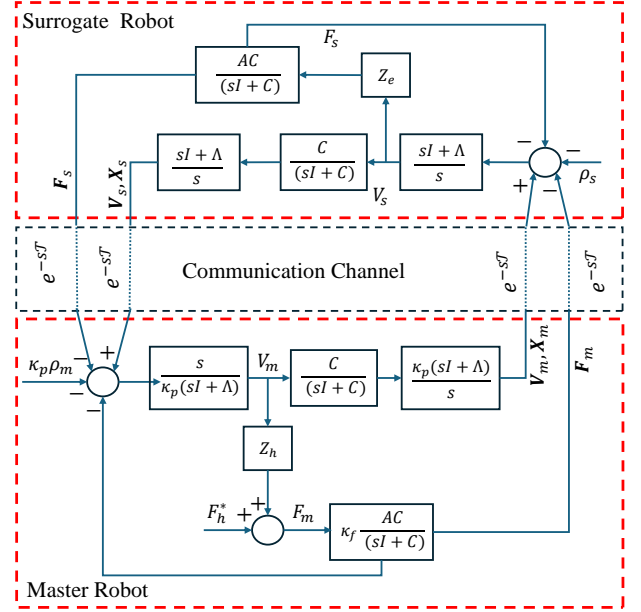


Fig. 5. Block diagram representation of dissimilar force-reflected bilateral teleoperation with arbitrary communication delay.

$$\mathcal{H}_{2m}(s) \stackrel{\text{def}}{=} (s\mathbf{I} + \Lambda) - s\mathbf{A}\mathbf{Z}_e(s) \quad (72)$$

where  $\mathbf{Z}_e = F_s(s)/V_s(s)$  and  $\mathbf{Z}_h(s) = (F_m(s) - F_h(s))/V_m(s)$ . A simplified model for a single DoF system is derived in [44].

### B. Transparency

Substituting (56) and (57) into (25) and (54), one can obtain,

$$\begin{aligned} \rho_s + \kappa_p \rho_m &= -\mathcal{C}^{-1}(\kappa_p \dot{V}_m + \dot{V}_s + \Lambda(\kappa_p V_m + V_s)) \\ &\quad - 2\mathcal{A}(\mathbf{F}_s + \kappa_f \mathbf{F}_m). \end{aligned} \quad (73)$$

Then, substituting (62) and (63) in (73), one can have,

$$-\mathbf{F}_m = \kappa_f^{-1} \mathbf{F}_s + \kappa_f^{-1} \kappa_p \mathcal{A}^{-1} \mathcal{C}^{-1} (s\mathbf{I} + \Lambda) \mathbf{V}_m + \frac{1}{2} \kappa_f^{-1} \rho_1 \quad (74)$$

with

$$\rho_1 \stackrel{\text{def}}{=} \mathcal{A}^{-1} [\mathcal{C}^{-1} (s\mathbf{I} + \Lambda) (\rho_v) + (\rho_s + \kappa_p \rho_m)]. \quad (75)$$

On the other hand, from Fig. 5 following holds,

$$\mathbf{V}_s = -\frac{s}{s\mathbf{I} + \Lambda} \mathcal{A} \mathbf{F}_s + \kappa_p \mathbf{V}_m + \frac{s}{s\mathbf{I} + \Lambda} \rho_2 \quad (76)$$

where,

$$\rho_2 \stackrel{\text{def}}{=} -\rho_s + \kappa_f [\rho_m - (V_{md} - V_m)]. \quad (77)$$

Then, (74) and (76) can be written in a compact form as,

$$\begin{bmatrix} -\mathbf{F}_m \\ -\mathbf{V}_s \end{bmatrix} = \underbrace{\begin{bmatrix} \underbrace{\kappa_f^{-1} \kappa_p \mathcal{A}^{-1} \mathcal{C}^{-1} (s\mathbf{I} + \Lambda)}_{g_{11}} & \kappa_f^{-1} \\ -\kappa_p & \underbrace{\frac{s}{s\mathbf{I} + \Lambda} \mathcal{A}}_{g_{22}} \end{bmatrix}}_G \begin{bmatrix} \mathbf{V}_m \\ \mathbf{F}_s \end{bmatrix}$$

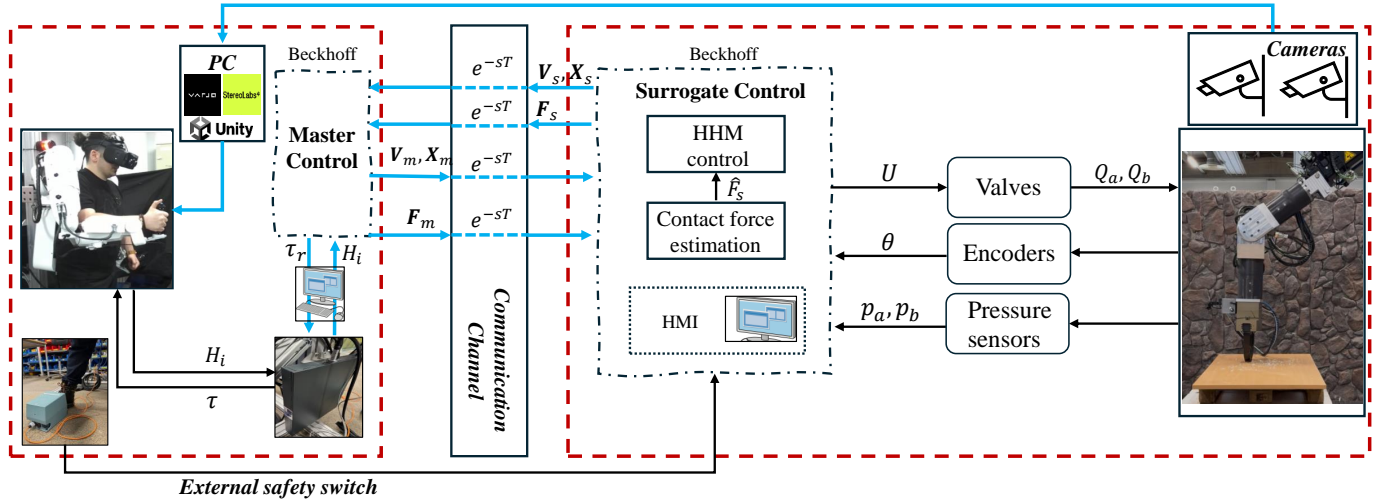


Fig. 6. Scheme of experiment setup; The teleoperation setup consists of master robot, master PC, master side Beckhoff, surrogate, surrogate PC, and surrogate side Beckhoff. All the blue lines demonstrate UDP communication, while black lines indicate control signals.

$$+ \underbrace{\begin{bmatrix} \frac{1}{2}\kappa_f^{-1}\rho_1 \\ s \\ -s\mathbf{I} + \Lambda\rho_2 \end{bmatrix}}_{\rho}. \quad (78)$$

The  $G$  matrix in (78) is referred to as the transparency matrix. For high-fidelity bilateral teleoperation with motion/force scaling, the ideal transparency matrix is [57]:

$$G_{\text{ideal}} = \begin{bmatrix} 0 & \kappa_f^{-1} \\ -\kappa_p & 0 \end{bmatrix}. \quad (79)$$

A comparison of the ideal transparency matrix in (79) with the actual matrix in (78) reveals that ideal transparency can be achieved when  $g_{11} = g_{12} = 0$ . However, this criterion is constrained by stability conditions. Consequently, perfect transparency and stability cannot be achieved simultaneously, and only a trade-off between the two can be satisfied. Nevertheless, by appropriately selecting the control gains, a good level of transparency can be achieved.

*Remark 3:* Nonzero values of  $g_{11}|_{F_s=0}$  in (78) indicate that the operator may experience a sticky sensation while operating the master robot during free motion. Conversely, nonzero values of  $g_{22}|_{V_m=0}$  suggest that during contact between the surrogate and the environment—where the master robot remains stationary—the surrogate will exhibit compliant behavior in response to external forces to ensure stability of the interaction.

*Remark 4:* The term  $g_{11}$  in (78) represents the scaled impedance of the surrogate as perceived by the human arm when there is no contact force ( $F_s = 0$ ). From  $g_{11}$ , it follows that,

$$\begin{aligned} \kappa_f^{-1}\kappa_p\mathcal{A}^{-1}\mathcal{C}^{-1}(s\mathbf{I} + \Lambda)\mathbf{V}_m &= \kappa_f^{-1}(\mathcal{A}^{-1}\mathcal{C}^{-1}(s\mathbf{I} + \Lambda))\mathbf{V}_s \\ &= \kappa_f^{-1}\mathbf{Z}_s, \end{aligned} \quad (80)$$

which indicates that during free motion, the force experienced by the human is equivalent to the scaled impedance of the surrogate. This concept is also illustrated in Fig. 1c.

## VII. EXPERIMENTAL RESULTS

This section is dedicated for comprehensive performance evaluation of the proposed method. Fig. 6 depicts the detail of the implementation setup.

### A. Experimental Setup

The conducted experiments consist of two main parts. The first part focuses on evaluating the performance of the proposed control algorithm under various conditions, including different position and force scaling factors—which directly influence the ranges of operational velocity and contact force—as well as under varying communication delays. To comprehensively assess the performance of the control scheme, we define the following evaluation metrics:

As can be seen from Fig. 6, our experimental setup is a real-world benchmark designed to rigorously test the proposed control scheme under challenging conditions. The 7-DoF haptic exoskeleton, as the master robot, introduces inherent uncertainties from its complex forearm and wrist mechanisms, including belts, ball screws, and cables. These are compounded by the nonlinear fluid dynamics governing the 6-DoF heavy-duty surrogate. The human operator interfaces with the system through haptic exoskeleton and VR-based active vision, together creating an immersive teleoperation experience representative of real-world industrial applications. This unique configuration not only can challenge the adaptability of the control scheme to mechanical, hydraulic, and network complexities but also evaluates its potential universality and reliability in high-stakes, heavy-duty operations.

The master-side control system is implemented on a Beckhoff CX5130 industrial PC with a 1 ms sampling rate. It communicates with the surrogate-side controller, which runs on a Beckhoff CX2030 unit, also operating at a 1 ms sampling rate. The surrogate robot is actuated through electrohydraulic servo valves with the following specifications: (1) base joint—Bosch 4WRPEH6 valve (12 dm<sup>3</sup>/min at  $\Delta p = 3.5$  MPa per notch), (2) lift and tilt joints—Bosch 4WRPEH10 valve (100 dm<sup>3</sup>/min

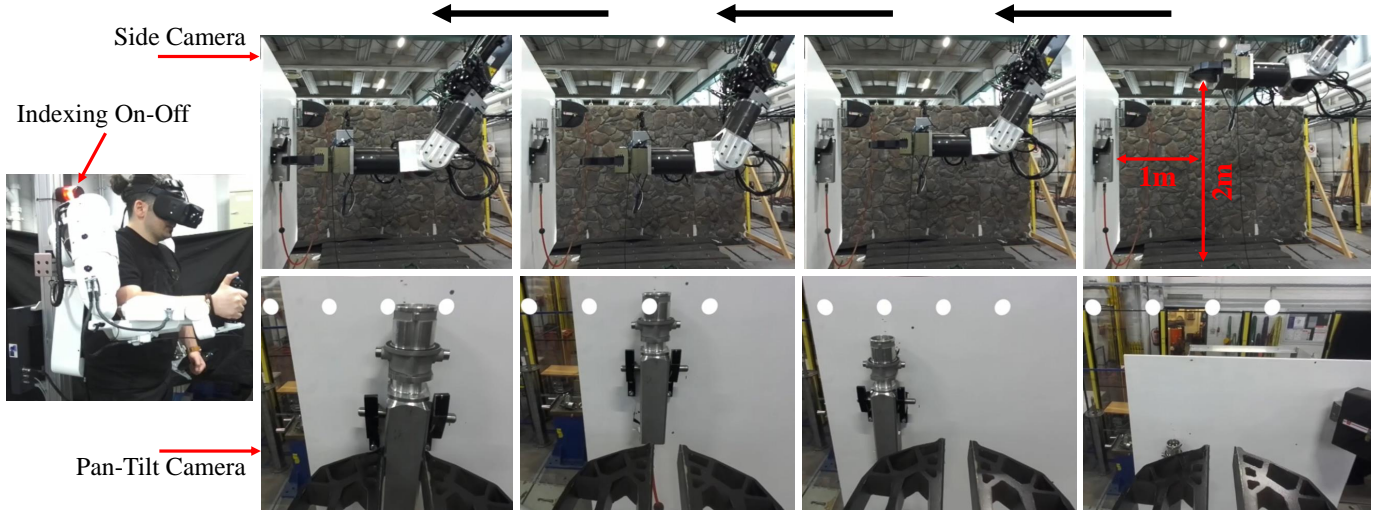


Fig. 7. Sequential steps of the free-motion experiment, shown from right to left. The surrogate, controlled by a human operator, approaches and grasps the target object. The top row displays the side camera view, while the bottom row shows the pan-tilt camera view—both providing essential visual feedback to support the operator’s task execution.

at  $\Delta p = 3.5$  MPa per notch), and (3) wrist joints—Bosch 4WRPEH6 valve (40 dm<sup>3</sup>/min at  $\Delta p = 3.5$  MPa per notch). Surrogate joint angles are measured using SICK AFS60 absolute encoders (18-bit resolution), and hydraulic pressures are acquired via Unix 5000 pressure transmitters with a maximum operating pressure of 25 MPa. Visual feedback is provided through ZED Mini stereo cameras operating at 60 fps with a resolution of  $2 \times 1280 \times 720$ . Egocentric viewpoint tracking is enabled by a pan-tilt mechanism synchronized with head movements in Unity via UDP communication. While the setup is agnostic to the VR hardware model, the Varjo XR-3 headset was used in this study.

To ensure the safety of both the human operator and robots during teleoperation, a three-level safety mechanism is implemented. First, in the Human-Machine Interface (HMI), the operator selects the teleoperation mode, only after which the teleoperation is ready to be enabled. Then, the operator has to grab the handle of the exoskeleton, which with its sensing signals, the second phase is enabled and the algorithm is ready for the next. Finally, the pedal shown in Fig. 6, which is an external signal to the control algorithm, enabled the indexing of the master robot. By releasing either pedal or handle of the exoskeleton, the actuators of the exoskeleton are deactivated and the surrogate switches to its local control mode. Such a multi-level safety setup removes the risk of unaware teleoperation connection and potential damage to either robots or the operator. It must be emphasized that, prior to enabling teleoperation, all essential configurations, including control modes and gain adjustments, position and force scaling, and system calibration, are managed through a HMI that has been entirely designed and developed in our laboratory using TwinCAT 3. The HMI is designed to be versatile, enabling communication with other industrial control systems through standardized interfaces. This facilitates integration into broader automation architectures, allowing the system to operate within existing industrial workflows.

### B. Scenarios of Experiments

- **Task Completion Time ( $\mathcal{T}$ ):** The total time required for the operator to execute the task illustrated in Fig. 7.
- **Maximum Tracking Error** of the displacement norm ( $\mathcal{N} = \|X_m\| - \|X_s\|$ ):

$$\mathcal{N}_{\max} = \max_{t \in [0, \mathcal{T}]} |\mathcal{N}(t)|$$

- **Root Mean Square Error (RMSE) of the Displacement Norm ( $\mathcal{N}_{rms}$ ):**

$$\mathcal{N}_{rms} = RMS(\mathcal{N}(t)) = \sqrt{\frac{1}{N} \sum_{i=1}^N \mathcal{N}_i^2}$$

- **Integral Absolute Error (IAE) of the Displacement Norm ( $\mathcal{N}_I$ ):**

$$\mathcal{N}_I = \int_0^{\mathcal{T}} |\mathcal{N}(t)| dt$$

This metric captures the total accumulated deviation in position error over the task duration.

- **Mean Absolute Error (MAE) of Velocity Tracking ( $\bar{V}$ ),** defined as the difference between the norm of the master and surrogate velocities:

$$\bar{V} = \frac{1}{N} \sum_{i=1}^N (\|V_m\|_i - \|V_s\|_i)$$

- **Position-Velocity Normalizing Index ( $\rho$ ),** which evaluates the relationship between the maximum position error and the maximum velocity:

$$\rho = \frac{\mathcal{N}_{\max}}{\|V_s\|_{\max}}$$

This index helps assess how well the surrogate can maintain accurate tracking under various velocity conditions.

- **Maximum and RMS of Force Tracking Error ( $\mathcal{F}_{\max}, \mathcal{F}_{rms}$ ),** evaluating the error between the master-side commanded force and the surrogate-side estimated

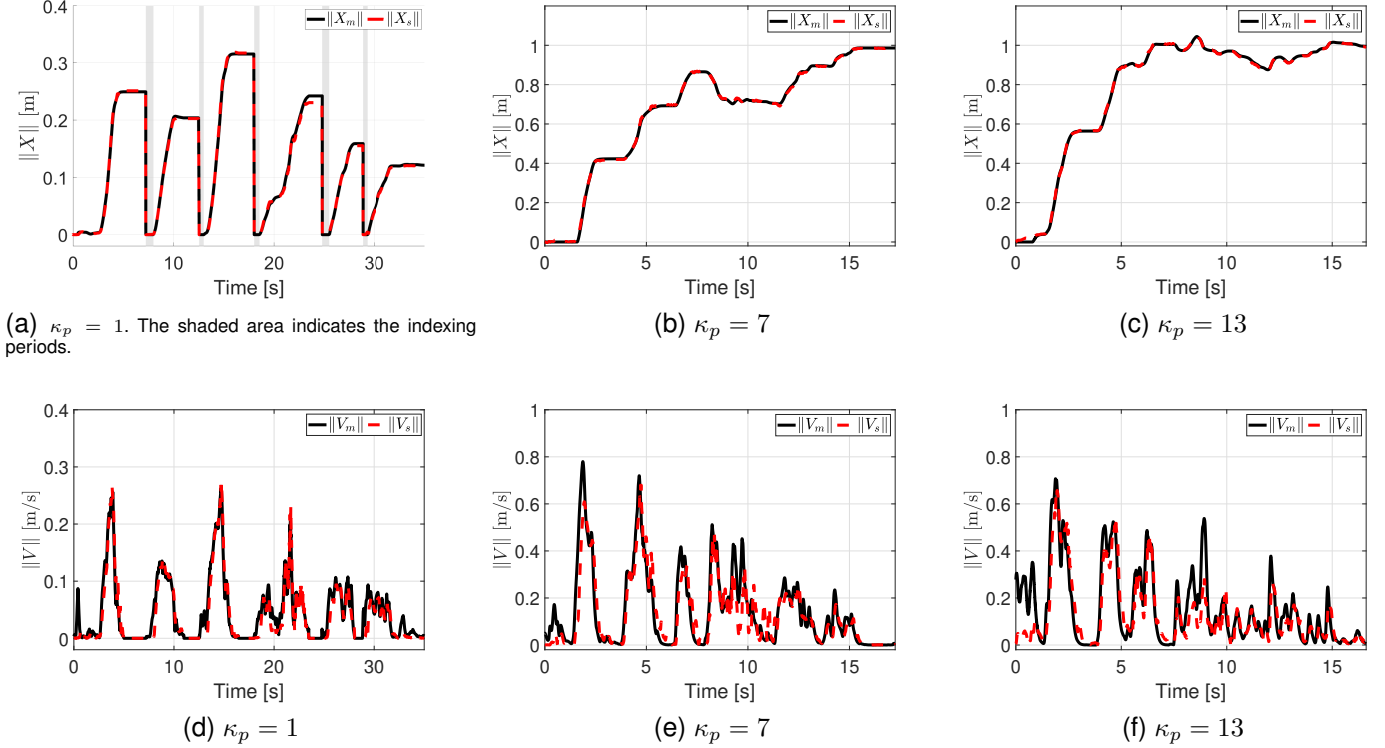


Fig. 8. Experimental results of the free-motion task under different motion scaling factors. (a)–(c) show the norm of position tracking, while (d)–(f) present the norm of velocity tracking.

TABLE I  
PERFORMANCE METRICS FOR DIFFERENT MOTION SCALING FACTORS.

Experiments	$\mathcal{T}$ [s]	$\mathcal{N}_{p,max}$ [m]	$\mathcal{N}_{p,rms}$ [m]	$\mathcal{N}_{p,I}$ [m·s]	$\bar{V}$ [m/s]	$\rho$	$\mathcal{N}_{o,max}$ [deg]	$\mathcal{N}_{o,rms}$ [deg]
$\kappa_p = 1$	35	0.011	0.0037	0.093	0.011	0.043	0.94	0.34
$\kappa_p = 7$	17.25	0.020	0.0052	0.068	0.04	0.03	0.820	0.43
$\kappa_p = 13$	16.6	0.029	0.0057	0.064	0.056	0.044	0.76	0.43
<i>Experiments below are conducted with delay and <math>\kappa_p = 3</math>:</i>								
Fixed delay $\mathcal{T}_f = 150$ ms	26.76	0.0430	0.0165	0.37	0.03	0.097	1.32	0.61
Time-varying delay $0 < \mathcal{T}_v < 150$ ms	21.47	0.035	0.011	0.2	0.038	0.047	1.41	0.63

applied force in the direction of interaction with  $\mathcal{F} = F_m(t) - F_s(t)$ :

$$\mathcal{F}_{\max} = \max_{t \in [0, \mathcal{T}]} |\mathcal{F}|, \quad \mathcal{F}_{\text{rms}} = \text{RMS}(\mathcal{F})$$

These metrics ensure a detailed and robust evaluation of the proposed control scheme under different scaling, time delay, and contact conditions. In the second set of experiments, we conducted a user study to evaluate the performance and usability of the proposed control scheme, the detail of which is provided in subsection VII-E.

In all experiments, the filter constant was set to  $\mathcal{C} = 35$ . For experiments without time delay, the force and position control gains were set to  $\mathcal{A} = 80 \times 10^{-5}$  and  $\Lambda = 12$ , respectively. In contrast, for experiments involving communication delay, the gains were adjusted to  $\mathcal{A} = 50 \times 10^{-5}$  and  $\Lambda = 3$  to satisfy the stability condition defined in (68), thereby achieving an optimal trade-off between maximum tolerable fixed delay and acceptable control accuracy. For the user study experiments, the control gains were set to  $\mathcal{A} = 80 \times 10^{-5}$  and  $\Lambda = 4$

to ensure smooth teleoperation and allow the surrogate to tolerate fast and high-jerk commands from participants, who are non-expert teleoperators. The local control gains for both the master and surrogate systems were configured identically to those reported in [51] and [52].

### C. Free Motion Performance Evaluation

In this section, we investigate three representative scaling factors in teleoperation experiments without communication delay: low ( $\kappa_p = 1$ ), medium ( $\kappa_p = 7$ ), and high ( $\kappa_p = 13$ ). For teleoperation under communication delay, we consider a scaling factor of  $\kappa_p = 3$  under two conditions: fixed delay  $\mathcal{T}_f = 150$  ms, and time-varying delay within the range  $0 < \mathcal{T}_v < 150$  ms. During each trial, the operator is instructed to approach a designated task board (Fig. 5), align the end-effector with the object of interest, and perform a grasping operation. The complete sequence of this free-motion task is illustrated in Fig. 7. The experimental results are presented in Fig. 8. Figs. 8a–8c plot the norm of the end-

effector position for each scale, while Figs. 8d–8f show the corresponding velocity norms. Across all cases, the proposed controller demonstrates stable tracking and accurate translation of the operator’s commands to the surrogate.

Under  $\kappa_p = 1$ , the operator required multiple indexing motions to reach the goal, primarily due to the mismatch between the limited workspace of the human arm and the extended reach of the surrogate. In contrast, with higher scaling factors, the operator was able to move the surrogate faster using smaller teleoperation commands. However, this increased mobility came at a perceptual cost. As the scale increases from 7 to 13, operator experienced a temporary mismatch between their proprioceptive sense of motion and the observed robot behavior through VR, which resulted in a longer time to think about how to accomplish the task. This phenomenon is evident in the only marginal improvement in execution time between  $\kappa_p = 7$  and  $\kappa_p = 13$ , despite the latter offering greater kinematic amplification. We posit that the observed discrepancy in perceptual adaptation stems from a form of sensorimotor mismatch: while the operator consciously understands the presence of motion scaling, their sensorimotor system temporarily resists reconciling slow proprioceptive input with fast visual feedback from the robot. This mismatch, although initially disorienting, tends to decrease over time with continued experience, and may be further alleviated by introducing longer adaptation phases.

Table I quantifies these observations. As expected, task execution time  $\mathcal{T}$  decreases with increasing scale due to faster end-effector velocities. However, the position tracking error increases accordingly: maximum error rises from 1.1 cm to 2.9 cm, and RMS error from 0.37 cm to 0.57 cm, as  $\kappa_p$  increases from 1 to 13. Despite this, the velocity-normalized error index  $\rho$  remains relatively consistent across all experiments, indicating that the tracking accuracy scales proportionally with motion speed, and the controller maintains a well-balanced performance. Furthermore, the controller maintained excellent velocity and orientation tracking performance, even under the high accelerations and velocities induced by large motion scaling factors in such a heavy-duty system. Fig. 9 demonstrates the result of system stability assessment in the presence of communication delay. The variable delay was generated using a uniformly distributed random process. In both scenarios, the system remains stable and task completion is achieved with acceptable accuracy. Metrics reported in Table I confirm that, although performance degrades modestly under delay, the controller maintains operational transparency and remains responsive to the human operator’s commands.

To further evaluate the performance of the proposed controller, the operator was instructed to perform a random motion in space, commanding both position and orientation changes of the end-effector. The results of this experiment with a scaling factor of  $\kappa_p = 4$  are illustrated in Fig. 10. Specifically, Fig. 10a displays the end-effector position trajectories, Fig. 10b shows the orientation tracking in terms of Euler angles, Fig. 10c presents the quaternion RMS error, Fig. 10d depicts the position RMS error, and Fig. 10e shows the norm of the end-effector velocity. The results demonstrate the excellent tracking performance of the proposed controller, with

orientation errors remaining below 2deg and position errors within 2 cm.

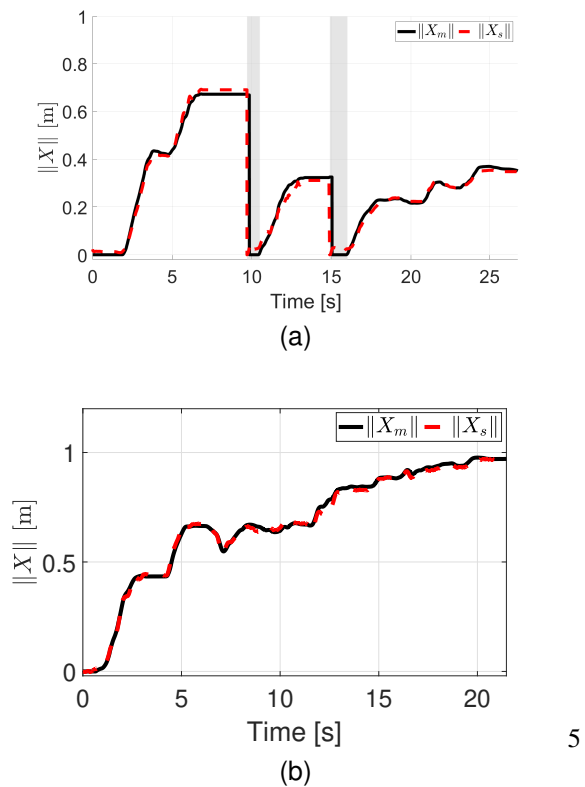


Fig. 9. Performance evaluation of the teleoperation system under communication delay with  $\kappa_p = 3$ . (a) Fixed communication delay  $T_f = 150$  ms. (b) Time-varying delay  $0 < T_v < 150$  ms.

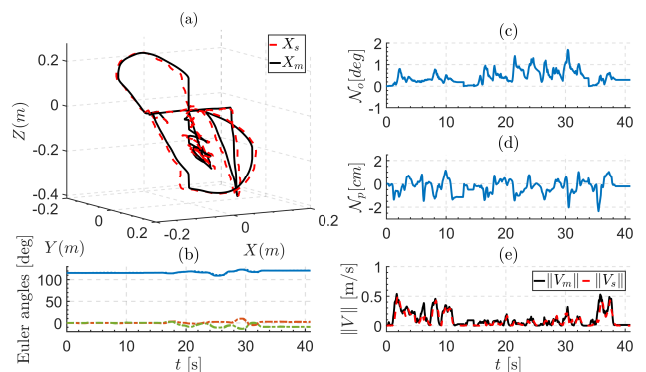


Fig. 10. Experimental results with  $\kappa_p = 4$ . (a) Position tracking; (b) orientation tracking in Euler angle representation; (c) quaternion RMS error; (d) position tracking error; (e) velocity tracking.

#### D. Contact-rich Performance Evaluation

In this section, the force-reflection and force-tracking capabilities of the teleoperation system are evaluated. To assess these functionalities, the operator was instructed to drive the surrogate, establish contact with a remote object, and then apply interaction forces upon sensing contact. The experimental procedure is illustrated in Fig. 12. These experiments were conducted with a motion scaling factor of  $\kappa_p = 2$  and varying

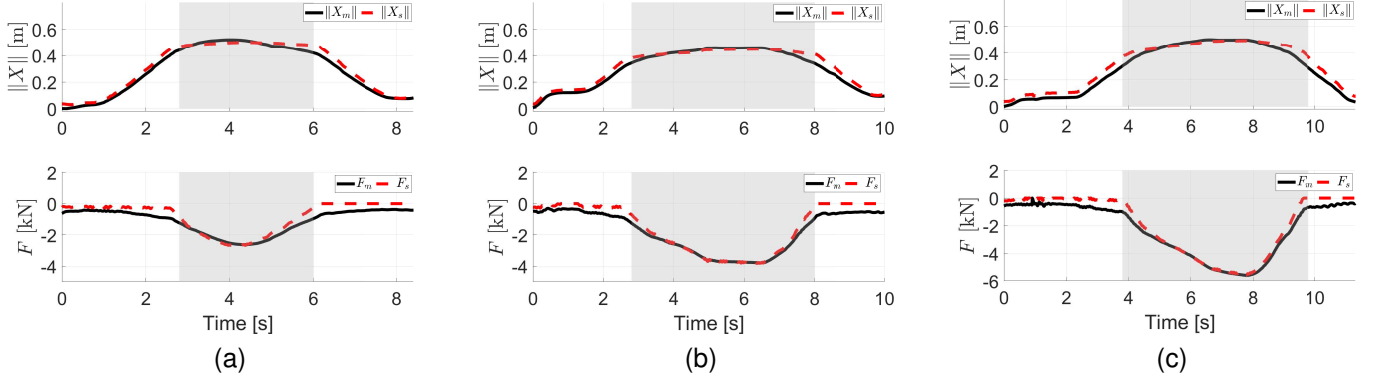


Fig. 11. Experimental evaluation of force-reflection and force-tracking performance in teleoperation with  $\kappa_p = 2$ . (a) Force and position tracking for  $\kappa_f = 500$ ; (b) for  $\kappa_f = 800$ ; (c) for  $\kappa_f = 1000$ .

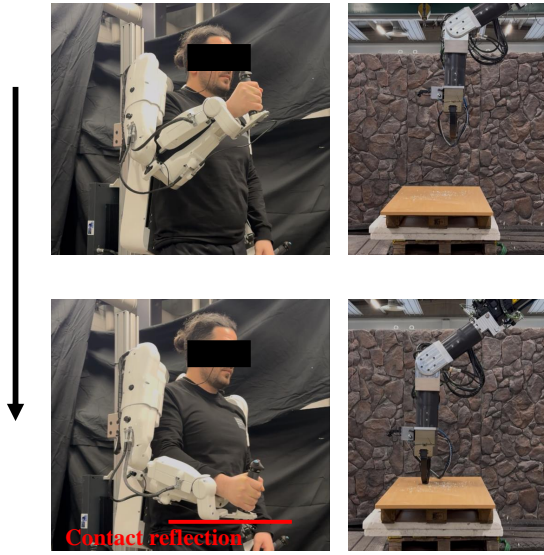


Fig. 12. Contact experiment sequences. The operator does not see the contact, and the contact is felt only by the reflection on the arm.

force scaling values of  $\kappa_f = 500, 800,$  and  $1000$ . The results are presented in Fig. 11. As shown, the forces applied by the operator are effectively transmitted through the system and exerted on the remote environment with high fidelity. These results demonstrate that human-applied forces can be amplified up to 1000 times, which is a significant achievement. In addition, contact experiments were conducted in the presence of both fixed and time-varying communication delays, using a force scaling factor of  $\kappa_f = 800$ . The results are shown in Fig. 13: Fig. 13a presents position and force tracking under a fixed delay, while Fig. 13b shows the same under a time-varying delay. These delayed experiments were performed over extended durations compared to the non-delayed ones to further investigate system stability and transparency. Despite the presence of considerable communication delay, the proposed control scheme maintained a favorable trade-off between transparency and stability.

A quantitative summary of the results is provided in Table II. For instance, with  $\kappa_f = 500$ , the maximum and RMS force

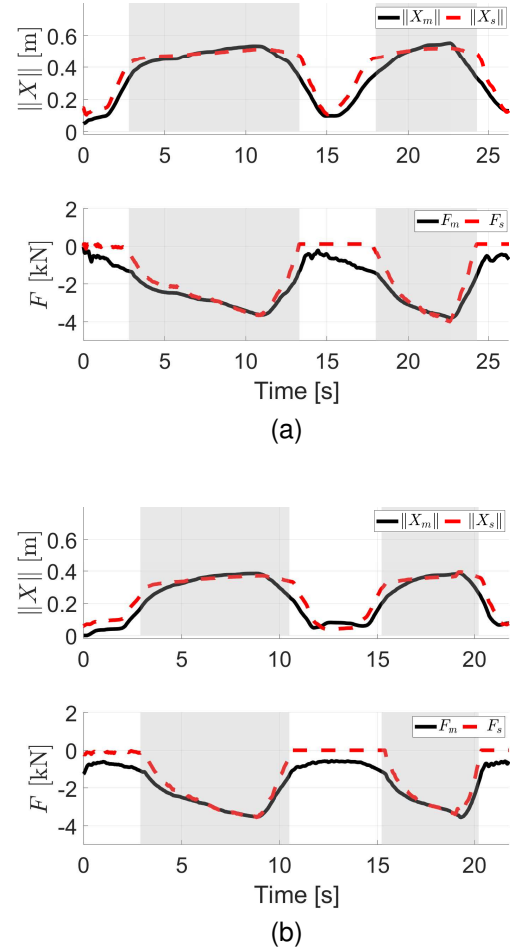


Fig. 13. Contact experiments under communication delay with  $\kappa_f = 800$  and  $\kappa_p = 2$ . (a) Position and force tracking with fixed delay  $\mathcal{T}_f = 150$  ms; (b) position and force tracking with time-varying delay  $0 < \mathcal{T}_v < 150$  ms.

errors reached 737 N and 387 N, respectively. When the force scaling was increased to  $\kappa_f = 1000$ , the maximum and RMS errors remained comparable at 848 N and 448 N, respectively—indicating robust tracking performance even under extreme amplification. As expected, the addition of delay de-

graded tracking performance to some extent. Nevertheless, the controller maintained stable execution and preserved a strong sense of transparency. Other metrics reported in Table II, such as position and orientation errors, further confirm the excellent performance of the controller in both delayed and non-delayed conditions.

*Remark 5:* It should be noted that both the human-applied forces and the contact forces at the remote site are estimated, which may introduce some inaccuracies—particularly on the master side. However, these estimation errors do not hinder the effectiveness of force reflection within the teleoperation system. As a result, the proposed force-sensor-less method offers a practical solution for real-world deployment, especially considering that conventional 6-DOF force/torque sensors are often fragile and susceptible to overloading .

TABLE II  
PERFORMANCE METRICS IN CONTACT TASKS UNDER DIFFERENT FORCE SCALING AND DELAY CONDITIONS.

Experiment	$\mathcal{N}_{p,rms}$ [m]	$\mathcal{N}_{o,rms}$ [deg]	$\mathcal{F}_{max}$ [N]	$\mathcal{F}_{rms}$ [N]
$k_f = 500$	0.0302	0.52	737.79	387.90
$k_f = 800$	0.0299	0.51	779.00	391.65
$k_f = 1000$	0.0408	0.45	848.60	448.25
<i>Experiments below are conducted with delay and <math>\kappa_f = 800</math>:</i>				
Fixed delay $\mathcal{T}_f = 150$ ms	0.0597	0.75	1638.73	676.80
Varying delay $0 < \mathcal{T}_v < 150$ ms	0.0508	0.74	1171.71	588.88

### E. User Study

To evaluate the SoE and usability of the proposed teleoperation system, we conducted a user study using an adapted version of the questionnaire from [58] for SoE assessment, alongside a custom-designed questionnaire to evaluate system usability. A total of 10 participants (9 male, 1 female) were took part in the study, shown in Fig. 14, and instructed to complete the same free motion task illustrated in Fig. 7 with  $\kappa_p = 2$ . To intentionally challenge the system’s robustness under non-expert operation, the training phase was deliberately minimal. Participants were briefly introduced to the system, including expected haptic and visual feedback, and were then given only 2–3 minutes to familiarize themselves with the haptic exoskeleton through self-guided exploration. Such user studies are rarely reported in the literature, particularly for bilateral teleoperation systems involving real-world HHMs, which are typically characterized by nonlinearities, delays, and high inertial dynamics. To the best of our knowledge, very few—if any—existing studies have demonstrated comparable usability in such complex settings. Conducting a user study with non-expert participants on a large-scale system of this kind is especially unique and requires a highly reliable and safe experimental setup to ensure both user safety and meaningful evaluation.

The participant pool included individuals with varying anthropometric profiles, particularly in height, thereby allowing us to assess the ergonomic and functional adaptability of the teleoperation setup across different operator physiques and



Fig. 14. User study experiment. The user is tasked to grasp the object on the white board.

genders. This diversity supports the generalizability of the proposed interface for a broad user population. Following the brief familiarization session, each participant performed the actual teleoperation task using the proposed setup. During this phase, the same performance metrics as in the prior experiments were recorded to enable quantitative evaluation of task execution. At the conclusion of the experiment, participants completed a standardized 7-point Likert-scale questionnaire (1 = strongly disagree, 7 = strongly agree) designed to assess the following core subjective dimensions:

- **Sense of Agency (SoA):** The participant’s perception of being in control of the surrogate’s movements.
- **Sense of Self-Location (SoSL):** The perceived spatial presence at the location of the surrogate.
- **Sense of Ownership (SoO):** The extent to which the surrogate was experienced as part of the participant’s own body.
- **System Usability:** The perceived intuitiveness and ease of use of the teleoperation interface.

Although SoO was not a primary focus of this study, we included two items related to ownership to explore whether high SoA and SoSL might induce a partial SoO. The completed questionnaire is provided in Table III.

The results of the questionnaire in Table III highlight the effectiveness of the proposed teleoperation setup in inducing a strong SoA, self-location, and usability—despite the system’s complexity and dissimilarity along with short familiarization period provided to the participants. Notably, participants reported a high level of control over the surrogate ( $Q_{A_2} = 6.50 \pm 0.71$ ) and a very low agreement with the statement that the robot moved autonomously ( $Q_{A_4} = 1.60 \pm 0.70$ ), indicating a robust SoA. Additionally, responses to  $Q_{A_1}$  and  $Q_{A_3}$  indicate that participants not only felt in control of the remote arm, but also experienced a tangible connection between their actions and the robot’s movements, likely facilitated by the distribution of scaled impedance of remote arm onto their own via the haptic exoskeleton. The high scores in the self-location category demonstrate that participants strongly felt as if they were spatially co-located with the surrogate. This is especially noteworthy given the asymmetry between the human operator’s body and the HHM, and it can be attributed to the use of egocentric viewpoint tracking and immersive VR

TABLE III  
QUESTIONNAIRE ITEMS FOR ASSESSING SOA, SoSL, SoO, AND  
USABILITY

Question	Statement	Score
<b>Category A: Sense of Agency</b>		
$Q_{A_1}$	It felt like I could control the remote arm as if it was my own arm.	$5.20 \pm 0.79$
$Q_{A_2}$	The movements of the remote arm were caused by my movements.	$6.50 \pm 0.71$
$Q_{A_3}$	I felt as if the movements of the remote arm were influencing my own movements.	$4.90 \pm 1.29$
$Q_{A_4}$	I felt as if the remote arm was moving by itself.	$1.60 \pm 0.70$
<b>Category L: Sense of Self-Location</b>		
$Q_{L_1}$	I felt as if I were located where the surrogate was.	$5.40 \pm 0.70$
$Q_{L_2}$	It felt as if I was seeing the environment through the eyes of the surrogate.	$6.00 \pm 0.82$
$Q_{L_3}$	I felt as if I was looking around the environment with my own head movements.	$6.10 \pm 1.20$
<b>Category O: Sense of Ownership</b>		
$Q_{O_1}$	I felt the remote body as if it were part of my own body.	$4.90 \pm 0.99$
$Q_{O_2}$	I felt the remote body as an extension of my own body.	$4.90 \pm 1.20$
<b>Category U: Usability</b>		
$Q_{U_1}$	I found the system very difficult to use.	$2.00 \pm 0.47$
$Q_{U_2}$	I felt comfortable using the system.	$5.70 \pm 0.82$
$Q_{U_3}$	I felt very confident using the system.	$6.10 \pm 0.88$
$Q_{U_4}$	The task required a lot of mental effort.	$2.70 \pm 1.34$

headsets. Although inducing a sense of ownership was not a primary objective, the responses to  $Q_{O_1}$  and  $Q_{O_2}$  (4.9 average) indicate that a moderate level of ownership was achieved. This is likely a result of the enhanced agency and self-location, both of which are known to contribute to the emergence of ownership in embodiment research. Interestingly, participants rated both the perception of the robot as a part of their body and as an extension of their body nearly equally. To derive an overall measure of the established level of SoE, the participants' questionnaire responses were linearly scaled to a normalized range of 0–100. As a result, the average normalized SoE score across all participants was found to be 76.4%, indicating a notably high level of embodiment. This is a particularly strong outcome considering the substantial dissimilarity and dynamic complexity of the master–surrogate system used in the experiments.

The usability results are particularly significant. Despite the use of a large-scale, heavy-duty surrogate, participants reported high comfort ( $Q_{U_2} = 5.70 \pm 0.82$ ) and confidence ( $Q_{U_3} = 6.10 \pm 0.88$ ) with low perceived difficulty ( $Q_{U_1} = 2.00 \pm 0.47$ ) and mental effort ( $Q_{U_4} = 2.70 \pm 1.34$ ). These scores underscore the intuitiveness and accessibility of the system—even for users with no prior experience without limitation to gender—further validating the ergonomic and cognitive effectiveness of the proposed control and interface design. Importantly, these subjective outcomes were achieved with a minimal familiarization session of only 2–3 minutes. Taken together, these findings provide compelling evidence for

TABLE IV  
RESULTS OF USER STUDY EXPERIMENTS

Metric	Mean $\pm$ Std
$\mathcal{N}_{p,\max}$ [cm]	$2.88 \pm 0.96$
$\mathcal{N}_{p,\text{rms}}$ [cm]	$1.09 \pm 0.36$
$\mathcal{N}_{o,\max}$ [deg]	$1.10 \pm 0.12$
$\mathcal{N}_{o,\text{rms}}$ [deg]	$0.66 \pm 0.05$
$\mathcal{N}_{v,\text{rms}}$ [m/s]	$0.058 \pm 0.016$
$\mathcal{T}$ [s]	$22.8 \pm 8.9$

the system's effectiveness in supporting natural, intuitive, and immersive control, for such a dissimilar teleoperation system.

To complement the subjective assessment, objective performance metrics are summarized in Table IV. The maximum position tracking error was limited to 2.88 cm, with an RMS error of 1.1 cm, with good orientation tracking performance. The mean end-effector velocity tracking error was 0.058 m/s, with an average task execution time of 22.8 s. Notably, these results were achieved despite reducing the position control gain  $\Lambda$  from 12 (used in optimal no-delay conditions) to 4—i.e., only 33% of the nominal gain. This confirms that the controller preserves stability even with significantly reduced gains, and that gain tuning primarily affects performance rather than stability. This is especially important in user studies, where robustness to suboptimal and variable commands from non-expert operators is essential. These findings further validate the system's real-world applicability and resilience.

## VIII. CONCLUSION

This study presented an immersive bilateral teleoperation framework with force reflection, tailored for highly dissimilar, beyond-human-scale master–surrogate systems without relying on physical force sensors. To address the fundamental challenge of human engagement in such teleoperation scenarios, we focused on enhancing the operator's SoE, specifically targeting the SoA and SoSL. High transparency was achieved through a robust and accurate control design capable of handling model uncertainties, input nonlinearities, and arbitrary time delays. Immersion was reinforced using a wearable haptic exoskeleton with distributed impedance rendering and a VR headset with egocentric head tracking. Theoretical analysis confirmed the semi-global uniform ultimate boundedness of the closed-loop system. Extensive real-world experiments validated the controller's robustness and performance across a wide range of motion and force scaling conditions, including up to 1:13 motion scaling and 1:1000 force scaling, along with fixed and time-varying communication delays up to 150 ms. Additionally, a comprehensive user study demonstrated the system's capability to establish a high SoE across all participants, with normalized embodiment scores 76.4%, regardless of gender-specific limitations. Participants also found the interface intuitive and easy to use, a noteworthy outcome given the scale and dynamics of the heavy-duty surrogate.

While this work provides a strong foundation for immersive bilateral teleoperation of beyond-human-scale robotic systems,

several promising directions remain for future development. A promising future direction includes mapping detected contact points on the surrogate body to anatomically equivalent regions on the human body, enhancing contextual awareness and embodiment. To enhance the efficiency and intuitiveness of the teleoperation experience, future work will focus on developing a shared control policy for the proposed force-reflected bilateral teleoperation system. Optimizing the location and control of the pan-tilt camera system may further reinforce first-person perspective and spatial congruence. Finally, integrating learning-from-demonstration techniques could facilitate skill transfer from humans to machines, advancing the autonomy of heavy-duty systems beyond current human capabilities.

#### APPENDIX A BOUNDEDNESS OF $p_{T_7}$

In the context of VDC, the augmented spatial velocity vector is defined as

$$\mathcal{V} = \mathcal{J} \dot{\mathbf{q}} \quad (\text{A.1})$$

where  $\dot{\mathbf{q}} \in \mathbb{R}^7$  is the vector of joint velocities, and  $\mathcal{J} \in \mathbb{R}^{49 \times 7}$  is the augmented Jacobian matrix that maps the joint velocity vector to the augmented spatial velocity vector.  $\mathcal{V} \in \mathbb{R}^{49}$  contains the spatial velocities of all frames in the decomposed system (for more details, refer to [54, Section 3.3.5]).

Similarly, the following expression maps the augmented spatial force vector of the decomposed system to the joint torque vector:

$$\boldsymbol{\tau} = \mathcal{J}^T \mathcal{F} \quad (\text{A.2})$$

where  $\mathcal{F} \in \mathbb{R}^{49}$  and  $\boldsymbol{\tau} \in \mathbb{R}^7$  denote the joint torque vector. Exploiting (A.1) and (A.2), the following expression for the human arm dynamics can be reconstructed from (8)–(10):

$$\boldsymbol{\tau}_m = \mathcal{J}^T \mathcal{M}_h \mathcal{J} \ddot{\mathbf{q}} + \mathcal{J}^T \mathcal{M}_h \dot{\mathcal{J}} \dot{\mathbf{q}} + \mathcal{J}^T \mathcal{C}_h + \boldsymbol{\tau}_h \quad (\text{A.3})$$

where  $\mathcal{M}_h \in \mathbb{R}^{49 \times 49}$  and  $\mathcal{C}_h \in \mathbb{R}^{49}$  are the augmented mass and damping matrices of the human arm,  $\boldsymbol{\tau}_h \in \mathbb{R}^7$  is the exogenous torque, and  $\boldsymbol{\tau}_m \in \mathbb{R}^7$  represents the human–robot interaction torque. In the same sense, we can write:

$$\boldsymbol{\tau}_{mr} = \mathcal{J}^T \hat{\mathcal{M}}_h \mathcal{J} \ddot{\mathbf{q}}_r + \mathcal{J}^T \hat{\mathcal{M}}_h \dot{\mathcal{J}} \dot{\mathbf{q}} + \mathcal{J}^T \hat{\mathcal{C}}_h + \hat{\boldsymbol{\tau}}_h \quad (\text{A.4})$$

The linear-in-parameter form for (A.4) can be written as:

$$\mathcal{Y}_h \hat{\boldsymbol{\Phi}}_h = \mathcal{J}^T \hat{\mathcal{M}}_h \mathcal{J} \ddot{\mathbf{q}}_r + \mathcal{J}^T \hat{\mathcal{M}}_h \dot{\mathcal{J}} \dot{\mathbf{q}} + \mathcal{J}^T \hat{\mathcal{C}}_h \quad (\text{A.5})$$

where  $\mathcal{Y}_h \in \mathbb{R}^{7 \times 49}$  is the augmented regression matrix and  $\hat{\boldsymbol{\Phi}}_h \in \mathbb{R}^{49}$  is the estimated augmented inertial parameter vector of the human arm. Note that Definition 3 can be used for  $\hat{\boldsymbol{\Phi}}_h$ .

By adding and subtracting  $\mathcal{J}^T \mathcal{M}_h \mathcal{J} \ddot{\mathbf{q}}_r$  to the right-hand side of (A.3) and substituting into  $(\boldsymbol{\tau}_{mr} - \boldsymbol{\tau}_m)$ , we obtain:

$$\boldsymbol{\tau}_{mr} - \boldsymbol{\tau}_m = \mathcal{Y}_h (\hat{\boldsymbol{\Phi}}_h - \boldsymbol{\Phi}_h) + \mathcal{J}^T \mathcal{M}_h \mathcal{J} (\ddot{\mathbf{q}}_r - \ddot{\mathbf{q}}) + \hat{\boldsymbol{\tau}}_h - \boldsymbol{\tau}_h. \quad (\text{A.6})$$

Assuming that the human arm and the robot have the same velocity at the end-effector, the VPF at frame  $\{T_7\}$  of the master robot can be written as:

$$\begin{aligned} p_{T_7} &= ({}^{T_7}V_r - {}^{T_7}V)^T ({}^{T_7}F_r - {}^{T_7}F) \\ &= (\dot{X}_{hr} - \dot{X}_{hr})^T (F_{mr} - F_m) \end{aligned} \quad (\text{A.7})$$

with

$$\dot{X}_h = V_m = \mathcal{J}_m \dot{\mathbf{q}}, \quad \dot{X}_{hr} = V_{mr} = \mathcal{J}_m \dot{\mathbf{q}}_r \quad (\text{A.8})$$

$$\boldsymbol{\tau}_m = \mathcal{J}_m^T F_m, \quad \boldsymbol{\tau}_{mr} = \mathcal{J}_m^T F_{mr} \quad (\text{A.9})$$

During physical human–robot interaction,  $p_{T_7}$  represents the power injected or absorbed by the human operator. Additionally, during the interaction phase, as the human grasps the handle of the exoskeleton, there is a continuous flow of power between the robot and the human arm, indicating that  $\|p_{T_7}\| \geq \varrho_m$ , where  $\varrho_m > 0$  is a small constant.

By substituting (A.8) and (A.9) into (A.7), we obtain:

$$p_{T_7} = (\dot{\mathbf{q}}_r - \dot{\mathbf{q}})^T (\boldsymbol{\tau}_{mr} - \boldsymbol{\tau}_m) \quad (\text{A.10})$$

Substituting (A.6) into (A.10) gives:

$$\begin{aligned} p_{T_7} &= (\dot{\mathbf{q}}_r - \dot{\mathbf{q}})^T \mathcal{Y}_h (\hat{\boldsymbol{\Phi}}_h - \boldsymbol{\Phi}_h) \\ &\quad + (\dot{\mathbf{q}}_r - \dot{\mathbf{q}})^T \mathcal{J}^T \mathcal{M}_h \mathcal{J} (\ddot{\mathbf{q}}_r - \ddot{\mathbf{q}}) \\ &\quad + (\dot{\mathbf{q}}_r - \dot{\mathbf{q}})^T (\hat{\boldsymbol{\tau}}_h - \boldsymbol{\tau}_h) \end{aligned} \quad (\text{A.11})$$

Taking the integral of  $p_{T_7}$  yields:

$$\begin{aligned} \lim_{t \rightarrow \infty} \int_0^t p_{T_7} dt &= \lim_{t \rightarrow \infty} \int_0^t (\dot{\mathbf{q}}_r - \dot{\mathbf{q}})^T \mathcal{Y}_h (\hat{\boldsymbol{\Phi}}_h - \boldsymbol{\Phi}_h) dt \\ &\quad + \lim_{t \rightarrow \infty} \int_0^t (\dot{\mathbf{q}}_r - \dot{\mathbf{q}})^T \mathcal{J}^T \mathcal{M}_h \mathcal{J} (\ddot{\mathbf{q}}_r - \ddot{\mathbf{q}}) dt \\ &\quad + \lim_{t \rightarrow \infty} \int_0^t (\dot{\mathbf{q}}_r - \dot{\mathbf{q}})^T (\hat{\boldsymbol{\tau}}_h - \boldsymbol{\tau}_h) dt \end{aligned} \quad (\text{A.12})$$

which leads to:

$$\lim_{t \rightarrow \infty} \int_0^t p_{T_7} dt \geq -\varrho_{0m} \quad (\text{A.13})$$

with

$$\begin{aligned} \varrho_{0m} &= \frac{\gamma}{2} \tilde{\boldsymbol{\Phi}}_h(0)^T \Gamma(\hat{\boldsymbol{\Phi}}_h(0)) \tilde{\boldsymbol{\Phi}}_h(0) \\ &\quad + \frac{1}{2} (\dot{\mathbf{q}}_r(0) - \dot{\mathbf{q}}(0))^T \mathcal{J}^T \mathcal{M}_h \mathcal{J} (\dot{\mathbf{q}}_r(0) - \dot{\mathbf{q}}(0)) \end{aligned} \quad (\text{A.14})$$

where  $\Gamma(\hat{\boldsymbol{\Phi}}_h(0))$  denotes the constant pullback of the Riemannian metric [53].

#### APPENDIX B PROOF OF LEMMA 4

By employing Definition 1, (42) and (48) along with  $V_s = V_T$ , the following holds for  $p_T$ ,

$$\begin{aligned} p_T &= ({}^T V_r - {}^T V)^T ({}^T F_r - {}^T F) \\ &= ({}^T V_r - {}^T V)^T N_c (f_{ed} - f_e) \\ &= ({}^T V_r - {}^T V)^T N_c M_e (\dot{V}_{sr} - \dot{V}_s) \\ &= (V_{sr} - V_s)^T M_e (\dot{V}_{sr} - \dot{V}_s) \end{aligned} \quad (\text{B.1})$$

which leads to,

$$\begin{aligned} \int_0^\infty p_T dt &= \int_0^\infty (V_{sr} - V_s)^T M_e (V_{sr} - V_s) dt \\ &\geq -0.5 (V_{sr}(0) - V_s(0))^T M_e (\dot{V}_{sr}(0) - \dot{V}_s(0)) \\ &\geq -\varrho_{0s}. \end{aligned} \quad (\text{B.2})$$

## REFERENCES

- [1] P. F. Hokayem and M. W. Spong, "Bilateral teleoperation: An historical survey," *Automatica*, vol. 42, no. 12, pp. 2035–2057, 2006.
- [2] H. Chen, P. Huang, and Z. Liu, "Mode switching-based symmetric predictive control mechanism for networked teleoperation space robot system," *IEEE/ASME Transactions on Mechatronics*, vol. 24, no. 6, pp. 2706–2717, 2019.
- [3] H. Su, C. Yang, G. Ferrigno, and E. De Momi, "Improved human-robot collaborative control of redundant robot for teleoperated minimally invasive surgery," *IEEE Robotics and Automation Letters*, vol. 4, no. 2, pp. 1447–1453, 2019.
- [4] M. Selvaggio, J. Cacace, C. Pacchierotti, F. Ruggiero, and P. R. Giordano, "A shared-control teleoperation architecture for nonprehensile object transportation," *IEEE Transactions on Robotics*, vol. 38, no. 1, pp. 569–583, 2021.
- [5] M. Suomalainen, J. Koivumäki, S. Lampinen, V. Kyrki, and J. Mattila, "Learning from demonstration for hydraulic manipulators," in *2018 IEEE/RSJ International Conference on Intelligent Robots and Systems (IROS)*. IEEE, 2018, pp. 3579–3586.
- [6] J. Mattila, J. Koivumäki, D. G. Caldwell, and C. Semini, "A survey on control of hydraulic robotic manipulators with projection to future trends," *IEEE/ASME Transactions on Mechatronics*, vol. 22, no. 2, pp. 669–680, 2017.
- [7] J. Zhang, E. Langbehn, D. Krupke, N. Katzakis, and F. Steinicke, "Detection thresholds for rotation and translation gains in 360 video-based telepresence systems," *IEEE transactions on visualization and computer graphics*, vol. 24, no. 4, pp. 1671–1680, 2018.
- [8] M. Slater and S. Wilbur, "A framework for immersive virtual environments (five): Speculations on the role of presence in virtual environments," *Presence: Teleoperators & Virtual Environments*, vol. 6, no. 6, pp. 603–616, 1997.
- [9] S. R. Ellis, "Presence of mind: a reaction to thomas sheridan's "further musings on the psychophysics of presence";," *Presence: Teleoperators & Virtual Environments*, vol. 5, no. 2, pp. 247–259, 1996.
- [10] E. B. Nash, G. W. Edwards, J. A. Thompson, and W. Barfield, "A review of presence and performance in virtual environments," *International Journal of human-computer Interaction*, vol. 12, no. 1, pp. 1–41, 2000.
- [11] M. Slater, "Place illusion and plausibility can lead to realistic behaviour in immersive virtual environments," *Philosophical Transactions of the Royal Society B: Biological Sciences*, vol. 364, no. 1535, pp. 3549–3557, 2009.
- [12] K. Kilteni, R. Groten, and M. Slater, "The sense of embodiment in virtual reality," *Presence: Teleoperators and Virtual Environments*, vol. 21, no. 4, pp. 373–387, 2012.
- [13] S. Falcone, G. Englebienne, J. Van Erp, and D. Heylen, "Toward standard guidelines to design the sense of embodiment in teleoperation applications: A review and toolbox," *Human-Computer Interaction*, vol. 38, no. 5–6, pp. 322–351, 2023.
- [14] M. E. Cabrera and J. P. Wachs, "A human-centered approach to one-shot gesture learning," *Frontiers in Robotics and AI*, vol. 4, p. 8, 2017.
- [15] D. Wei, B. Huang, and Q. Li, "Multi-view merging for robot teleoperation with virtual reality," *IEEE Robotics and Automation Letters*, vol. 6, no. 4, pp. 8537–8544, 2021.
- [16] X. Cheng, J. Li, S. Yang, G. Yang, and X. Wang, "Open-television: Teleoperation with immersive active visual feedback," *arXiv preprint arXiv:2407.01512*, 2024.
- [17] V. Girbes-Juan, V. Schettino, Y. Demiris, and J. Tornero, "Haptic and visual feedback assistance for dual-arm robot teleoperation in surface conditioning tasks," *IEEE Transactions on Haptics*, vol. 14, no. 1, pp. 44–56, 2020.
- [18] K. Li, R. Bacher, S. Schmidt, W. Leemans, and F. Steinicke, "Reality fusion: Robust real-time immersive mobile robot teleoperation with volumetric visual data fusion," in *2024 IEEE/RSJ International Conference on Intelligent Robots and Systems (IROS)*. IEEE, 2024, pp. 8982–8989.
- [19] F. De Pace, G. Gorjup, H. Bai, A. Sanna, M. Liarokapis, and M. Billinghurst, "Leveraging enhanced virtual reality methods and environments for efficient, intuitive, and immersive teleoperation of robots," in *2021 IEEE International Conference on Robotics and Automation (ICRA)*. IEEE, 2021, pp. 12 967–12 973.
- [20] P. Stotko, S. Krumpfen, M. Schwarz, C. Lenz, S. Behnke, R. Klein, and M. Weinmann, "A vr system for immersive teleoperation and live exploration with a mobile robot," in *2019 IEEE/RSJ International Conference on Intelligent Robots and Systems (IROS)*. IEEE, 2019, pp. 3630–3637.
- [21] F. Huang, X. Yang, T. Yan, and Z. Chen, "Telepresence augmentation for visual and haptic guided immersive teleoperation of industrial manipulator," *ISA transactions*, vol. 150, pp. 262–277, 2024.
- [22] S. Sirouspour and A. Shahdi, "Model predictive control for transparent teleoperation under communication time delay," *IEEE Transactions on Robotics*, vol. 22, no. 6, pp. 1131–1145, 2006.
- [23] N. Feizi, R. V. Patel, M. R. Kermani, and S. F. Atashzar, "Adaptive wave reconstruction through regulated-bmflc for transparency-enhanced telerobotics over delayed networks," *IEEE Transactions on Robotics*, vol. 38, no. 5, pp. 2928–2942, 2022.
- [24] D. A. Lawrence, "Stability and transparency in bilateral teleoperation," *IEEE transactions on robotics and automation*, vol. 9, no. 5, pp. 624–637, 1993.
- [25] K. Hashtrudi-Zaad and S. E. Salcudean, "Transparency in time-delayed systems and the effect of local force feedback for transparent teleoperation," *IEEE Transactions on Robotics and Automation*, vol. 18, no. 1, pp. 108–114, 2002.
- [26] Z. Chen, F. Huang, W. Sun, J. Gu, and B. Yao, "Rbf-neural-network-based adaptive robust control for nonlinear bilateral teleoperation manipulators with uncertainty and time delay," *Ieee/Asme Transactions on Mechatronics*, vol. 25, no. 2, pp. 906–918, 2019.
- [27] S. Guo, Z. Liu, J. Yu, P. Huang, and Z. Ma, "Adaptive practical fixed-time synchronization control for bilateral teleoperation system with prescribed performance," *IEEE Transactions on Circuits and Systems II: Express Briefs*, vol. 69, no. 3, pp. 1243–1247, 2021.
- [28] Z. Chen, F. Huang, W. Chen, J. Zhang, W. Sun, J. Chen, J. Gu, and S. Zhu, "Rbfnn-based adaptive sliding mode control design for delayed nonlinear multilateral telerobotic system with cooperative manipulation," *IEEE Transactions on Industrial Informatics*, vol. 16, no. 2, pp. 1236–1247, 2019.
- [29] Z. Chen, F. Huang, C. Yang, and B. Yao, "Adaptive fuzzy backstepping control for stable nonlinear bilateral teleoperation manipulators with enhanced transparency performance," *IEEE transactions on industrial electronics*, vol. 67, no. 1, pp. 746–756, 2019.
- [30] F. Huang, X. Yang, D. Mei, and Z. Chen, "Unified contact model and hybrid motion/force control for teleoperated manipulation in unknown environments," *IEEE/ASME Transactions on Mechatronics*, 2024.
- [31] T. Slama, A. Trevisani, D. Aubry, R. Oboe, and F. Kratz, "Experimental analysis of an internet-based bilateral teleoperation system with motion and force scaling using a model predictive controller," *IEEE Transactions on Industrial Electronics*, vol. 55, no. 9, pp. 3290–3299, 2008.
- [32] F. Ferraguti, M. Bonfe, C. Fantuzzi, and C. Secchi, "Optimized power modulation in wave-based bilateral teleoperation," *IEEE/ASME Transactions on Mechatronics*, vol. 26, no. 1, pp. 276–287, 2020.
- [33] M. Jorda, M. Vulliez, and O. Khatib, "Local autonomy-based haptic-robot interaction with dual-proxy model," *IEEE Transactions on Robotics*, vol. 38, no. 5, pp. 2943–2961, 2022.
- [34] T. Kastritsi, T. P. Semetzidis, and Z. Doulgeri, "Passive bilateral surgical teleoperation with rcm and spatial constraints in the presence of time delays," *IEEE Transactions on Robotics*, 2024.
- [35] S. Sirouspour, "Modeling and control of cooperative teleoperation systems," *IEEE Transactions on Robotics*, vol. 21, no. 6, pp. 1220–1225, 2005.
- [36] D. Sun, Q. Liao, and A. Loutfi, "Single master bimanual teleoperation system with efficient regulation," *IEEE Transactions on Robotics*, vol. 36, no. 4, pp. 1022–1037, 2020.
- [37] S. Tafazoli, S. E. Salcudean, K. Hashtrudi-Zaad, and P. D. Lawrence, "Impedance control of a teleoperated excavator," *IEEE Transactions on Control Systems Technology*, vol. 10, no. 3, pp. 355–367, 2002.
- [38] V. Banthia, K. Zareinia, S. Balakrishnan, and N. Sepehri, "A lyapunov stable controller for bilateral haptic teleoperation of single-rod hydraulic actuators," *Journal of Dynamic Systems, Measurement, and Control*, vol. 139, no. 11, p. 111001, 2017.
- [39] K. Zareinia, N. Sepehri, and Q. Wu, "A lyapunov controller for stable haptic manipulation of hydraulic actuators," *International Journal of Robust and Nonlinear Control*, vol. 22, no. 3, pp. 241–261, 2012.
- [40] X. Liang, Z. Yao, W. Deng, and J. Yao, "Adaptive neural network finite-time tracking control for uncertain hydraulic manipulators," *IEEE/ASME Transactions on Mechatronics*, 2024.
- [41] Z. Xu, W. Deng, H. Shen, and J. Yao, "Extended-state-observer-based adaptive prescribed performance control for hydraulic systems with full-state constraints," *IEEE/ASME Transactions on Mechatronics*, vol. 27, no. 6, pp. 5615–5625, 2022.
- [42] J. Koivumäki, W.-H. Zhu, and J. Mattila, "Energy-efficient and high-precision control of hydraulic robots," *Control Engineering Practice*, vol. 85, pp. 176–193, 2019.

- [43] J. Koivumäki and J. Mattila, “Stability-guaranteed impedance control of hydraulic robotic manipulators,” *IEEE/ASME Transactions On Mechatronics*, vol. 22, no. 2, pp. 601–612, 2016.
- [44] S. Lampinen, J. Koivumäki, W.-H. Zhu, and J. Mattila, “Force-sensorless bilateral teleoperation control of dissimilar master–slave system with arbitrary scaling,” *IEEE Transactions on Control Systems Technology*, vol. 30, no. 3, pp. 1037–1051, 2021.
- [45] S. Lampinen, J. Koivumäki, and J. Mattila, “Full-dynamics-based bilateral teleoperation of hydraulic robotic manipulators,” in *2018 IEEE 14th International Conference on Automation Science and Engineering (CASE)*. IEEE, 2018, pp. 1343–1350.
- [46] S. Luo, M. Cheng, R. Ding, F. Wang, B. Xu, and B. Chen, “Human–robot shared control based on locally weighted intent prediction for a teleoperated hydraulic manipulator system,” *IEEE/ASME Transactions on Mechatronics*, vol. 27, no. 6, pp. 4462–4474, 2022.
- [47] S. Lampinen, J. Koivumäki, and J. Mattila, “Bilateral teleoperation of a hydraulic robotic manipulator in contact with physical and virtual constraints,” in *Fluid Power Systems Technology*, vol. 51968. American Society of Mechanical Engineers, 2018, p. V001T01A021.
- [48] R. Ding, M. Cheng, Z. Han, F. Wang, and B. Xu, “Human-machine interface for a master-slave hydraulic manipulator with vision enhancement and auditory feedback,” *Automation in Construction*, vol. 136, p. 104145, 2022.
- [49] P. Garrec, “Design of the arm exoskeleton able achieving torque control using ball screw and cable mechanism,” in *Wearable Robotics*. Elsevier, 2020, pp. 45–66.
- [50] T. Z. Zhao, V. Kumar, S. Levine, and C. Finn, “Learning fine-grained bimanual manipulation with low-cost hardware,” *arXiv preprint arXiv:2304.13705*, 2023.
- [51] M. Hejrati and J. Mattila, “Physical human–robot interaction control of an upper limb exoskeleton with a decentralized neuroadaptive control scheme,” *IEEE Transactions on Control Systems Technology*, 2023.
- [52] —, “Orchestrated robust controller for precision control of heavy-duty hydraulic manipulators,” *IEEE Transactions on Automation Science and Engineering*, vol. 22, pp. 14 284 – 14 305, 2025.
- [53] —, “Decentralized nonlinear control of redundant upper limb exoskeleton with natural adaptation law,” in *2022 IEEE-RAS 21st International Conference on Humanoid Robots (Humanoids)*. IEEE, 2022, pp. 269–276.
- [54] W.-H. Zhu, *Virtual decomposition control: toward hyper degrees of freedom robots*. Springer Science & Business Media, 2010, vol. 60, section 3.3.5.
- [55] K. P. Tee, S. S. Ge, and E. H. Tay, “Barrier lyapunov functions for the control of output-constrained nonlinear systems,” *Automatica*, vol. 45, no. 4, pp. 918–927, 2009.
- [56] M. Hejrati and J. Mattila, “Impact-resilient orchestrated robust controller for heavy-duty hydraulic manipulators,” *IEEE/ASME Transactions on Mechatronics*, 2025.
- [57] B. Hannaford, “A design framework for teleoperators with kinesthetic feedback,” *IEEE transactions on Robotics and Automation*, vol. 5, no. 4, pp. 426–434, 1989.
- [58] M. Gonzalez-Franco and T. C. Peck, “Avatar embodiment. towards a standardized questionnaire,” *Frontiers in Robotics and AI*, vol. 5, p. 74, 2018.



**Mahdi Hejrati** received his M.Sc. degree in 2021 from Sharif University of Technology (SUT), Tehran, Iran. He is currently a PhD student at the unit of Automation Technology and Mechanical Engineering, Tampere University, Tampere, Finland. His research interests include nonlinear model-based control, physical human-robot interaction, and human-inspired control.



**Pauli Mustalahti** Pauli Mustalahti received his M.Sc. degree in engineering from the Tampere University of Technology in 2016 and his D.Sc. (Tech.) in Automation Science and Engineering from the Tampere University in 2023.

He is a researcher in the Automation Technology and Mechanical Engineering, Tampere University, Tampere, Finland. His research interests include nonlinear model-based control of robotic manipulators.



**Jouni Mattila** Dr. Tech. received his M.Sc. (Eng.) in 1995 and Dr. Tech. in 2000, both from Tampere University of Technology (TUT), Tampere, Finland. He is currently a Professor of machine automation with the unit of Automation Technology and Mechanical Engineering, Tampere University. His research interests include machine automation, nonlinear model-based control of robotic manipulators and energy-efficient control of heavy-duty mobile manipulators.